UNIVERSITY OF CALIFORNIA

SANTA CRUZ

SEARCH FOR TIME-DEPENDENT CP-VIOLATION IN $B^0 \to \rho^0\gamma$ TRANSITIONS

A dissertation submitted in partial satisfaction of the
requirements for the degree of

DOCTOR OF PHILOSOPHY

in

PHYSICS

by

Alfonso J. Martinez

March 2012

The dissertation of Alfonso J. Martinez
is approved:

Professor Bruce Schumm, Chair

Professor Abraham Seiden

Professor Jason Nielsen

Tyrus Miller
Vice Provost and Dean of Graduate Studies

Contents

List of Figures

List of Tables

Abstract

Search for Time-dependent CP-Violation in $B^0 \to \rho^0\gamma$ Transitions

by

Alfonso J. Martinez

This thesis presents progress made on an experimental study of radiative B^0 meson decays to the final state $\rho^0\gamma$ using data collected at the $\Upsilon(4S)$ resonance at the *BABAR* detector at the PEP-II e^+e^- collider at SLAC. Making use of the full data set collected at the *BABAR* detector of 465 million $B\overline{B}$ pairs we have done a preliminary measurement of the time-dependent CP-violation parameters S and C in $B^0 \to \rho^0\gamma$ decays, finding $S = 0.38 \pm 0.54 \pm 0.38$ and $C = 0.79 \pm 0.51 \pm 0.37$, where the uncertainties are statistical and systematic, respectively.

Chapter 1

Introduction

This thesis describes progress towards an experimental study of the time-dependent CP-violation (TDCPV) parameters S and C in $B^0 \to \rho^0\gamma$ decays using the 465 million $B\overline{B}$ decays observed between October 1999 and September 2007 in the *BABAR* detector at the SLAC National Accelerator Laboratory at Stanford.

The decay $B^0 \to \rho^0\gamma$ is an exclusive channel of the $b \to d\gamma$ process. Within the Standard Model (SM) of particle physics these flavor-changing-neutral-current

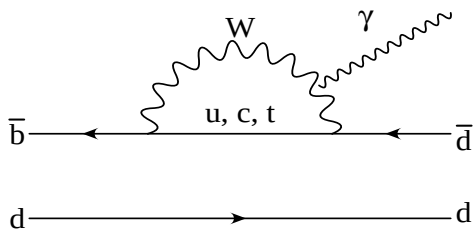

Figure 1.1: Feynman diagram for a $b \to d\gamma$ transition

(FCNC) $b \to d\gamma$ transitions are forbidden at tree level; the leading-order FCNC processes are one-loop electroweak penguin diagrams as shown in Figure 1.1. Here, the top is the dominant virtual quark contribution to the loop. Therefore, measurements of these processes provide information on the Cabibbo-Kobayashi-Maskawa (CKM) matrix element V_{td}. In the context of theories beyond the SM, new virtual particles appearing in the loop could lead to measurable new physics (NP) effects on experimental observables such as branching fractions and time-dependent CP-asymmetries such as S and C (to be discussed in Section 3.1.3) [1]. In particular, within the SM, where the top quark is the dominant virtual particle contribution in the loop, the decay amplitude has a weak phase that cancels the phase in the mixing; consequently S vanishes. Observing a non-zero value of S would indicate NP effects.

TDCPV parameters in $B^0 \to K^0_s\pi^0\gamma$ decays as well as the $B^0 \to \rho^0\gamma$ branching fractions have been measured at both BELLE [2][3] and *BABAR* [4][5]. In 2007 BELLE measured the CP-violating parameters in $B^0 \to \rho^0\gamma$ decays [6]. Currently, measurements of $b \to d\gamma$ branching fractions and CP-violating parameters are consistent with the SM; however, the constraints on S come only from a single BELLE measurement. This thesis documents work towards an independent constraint from *BABAR*.

BELLE	
$\mathcal{B}(B \to (\rho/\omega)\gamma)$ [2]	$(1.32^{+0.34}_{-0.31}(stat)^{+0.1}_{-0.09}(sys)) \times 10^{-6}$
$S_{B^0 \to K^0_s \pi^0 \gamma}$ [3]	$-0.10 \pm 0.31(sys) \pm 0.07(stat)$
$C_{B^0 \to K^0_s \pi^0 \gamma}$ [3]	$-0.20 \pm 0.20(sys) \pm 0.06(stat)$
BABAR	
$\mathcal{B}(B \to (\rho/\omega)\gamma)$ [4]	$(1.25^{+0.25}_{-0.24}(stat) \pm 0.09(sys)) \times 10^{-6}$
$S_{B^0 \to K^0_s \pi^0 \gamma}$ [5]	$0.9 \pm 1.0(stat) \pm 0.2(sys)$
$C_{B^0 \to K^0_s \pi^0 \gamma}$ [5]	$-1.0 \pm 0.5(stat) \pm 0.2(sys)$

Table 1.1: CP-violation parameter and branching fraction measurement results from *BABAR* and BELLE.

1.1 The Standard Model

The Standard Model is a quantum field theory of quarks, leptons, bosons, and the interactions between them. The strong, weak and electromagnetic forces correspond to the local gauge symmetry of the SM Lagrangian density under the combined group

$$SU(3)_{\text{color}} \otimes SU(2)_{\text{isospin}} \otimes U(1)_{\text{hypercharge}}.$$

There is an associated vector gauge boson that mediates the interaction for each generator of the group. The formal details of the interactions between the various particles were spelled out in the 1960's [7][8][9][10].

Including the symmetry-breaking Higgs field the SM has withstood every experimental test to which it is been subjected in the past 50 years. However, it has nothing to say about most of the density of the known universe, gravity, explain why there are three generations of matter, why elementary particles have the relative masses they do or why the relative strengths of the interactions between

them are what they are. The Higgs boson has yet to be discovered and there is no evidence that links the SM with what may lie beyond it. Furthermore, while the SM does incorporate known CP-violation effects, it fails to explain the observed matter antimatter asymmetry in the universe. Therefore there is a possibility that NP effects may be seen in the $B \to \rho\gamma$ radiative penguin decays of interest in this study. New virtual particles may appear in the loop, coupled to the heavy quarks, giving insight to the missing pieces of the current Standard Model.

1.2 The CKM Matrix

All charged-current weak interactions among the quarks are modified by the $3\times$ 3 unitary CKM matrix named after Cabibbo, Kobayashi, and Maskawa [11] [12]. The matrix mediates the mixing of the three quark generations. A consequence of the CKM couplings between the $W^{\pm}$ bosons and the fermions is that the physical coupling values may be complex; therefore CP may not be a good symmetry of the Lagrangian. The single complex phase leads to an irreducible phase in the Lagrangian that can manifest CP-violation. The information of the complex phases is contained in the CKM matrix. The Wolfenstein parametrization of the CKM matrix [13], to order λ^3, is shown in Equation 1.1. The measurements of weak processes that include the interference of transitions between all three quark generations, such as interference between decays with and without mixing, will manifest CP-violation, if it is present.

$$V_{ij} = \begin{array}{c} \\ u \\ c \\ t \end{array} \begin{array}{c} \begin{array}{ccc} d & s & b \end{array} \\ \begin{pmatrix} 1-\frac{1}{2}\lambda^2 & \lambda & A\lambda^3(\rho - i\eta) \\ -\lambda & 1-\frac{1}{2}\lambda^2 & A\lambda^2 \\ A\lambda^3(1-\rho-i\eta) & -A\lambda^2 & 1 \end{pmatrix} \end{array} \tag{1.1}$$

1.3 Search for New Physics in $b \to d(s)\gamma$ Transitions

Long-distance quantum chromodynamic (QCD) effects make it difficult to directly measure the CKM matrix elements V_{td} and V_{ts}. Looking instead at $|V_{td}|/|V_{ts}|$ eliminates these difficulties, as is done in $B_{d(s)}$-mixing and branching fraction comparisons. The long distance effects cancel out, and NP may be manifest in differences between independent measurements of this ratio. B-mixing and radiative $b \to d(s)\gamma$ branching fraction measurements have been carried out at both *BABAR* and BELLE, constraining these SM parameters.

Another, independent, method to further constrain SM parameters is the investigation of CP-violation in time-dependent measurements which is the subject of this study. The SM predicts some direct CP-violation but an observation of values that differ from the expectation would indicate NP effects.

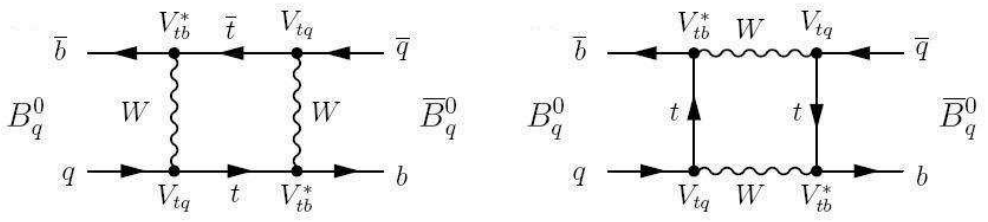

Figure 1.2: First-order box diagrams for B-mixing

1.3.1 B^0-Mixing

The first-order diagrams in $B_{d(s)}$-mixing are the box diagrams shown in Figure 1.2. As in radiative penguin $b \to d(s)\gamma$ transitions, measurements of these processes provide information about the CKM matrix elements V_{tq}.

B_d-mixing was first observed at ARGUS [14], and the mass difference Δm_d between the heavy and light B_d eigenstates has been measured many times since. With the 2006 discovery of B_s-mixing at the Tevatron, a precise constraint can be placed on $|V_{td}|/|V_{ts}|$ from B-mixing [15].

$$\left|\frac{V_{td}}{V_{ts}}\right| = \xi\sqrt{\frac{\Delta m_d m_{B_s^0}}{\Delta m_s m_{B^0}}} = 0.2060 \pm 0.0007(\text{stat})^{+0.0087}_{-0.0060}(\text{sys}). \tag{1.2}$$

This can in turn be used as a comparison point for radiative penguin branching fraction measurements of the same CKM element ratio. Since NP is likely to show up differently in radiative penguin and B-mixing diagrams, comparison of effective $|V_{td}|/|V_{ts}|$ from both channels is a sensitive test of NP.

1.3.2 Radiative Penguin Branching Fractions

One method of extracting the $|V_{td}|/|V_{ts}|$ ratio from $B \to (\rho/\omega)\gamma$ and $B \to K^*\gamma$ is shown in the following expression [16]:

$$\frac{\mathcal{B}(B \to (\rho/\omega)\gamma)}{\mathcal{B}(B \to K^*\gamma)} = \left|\frac{V_{td}}{V_{ts}}\right|^2 \left(\frac{1 - m^2_{\rho,\omega}/M^2_B}{1 - m^2_{K^*}/M^2_B}\right)^3 \zeta^2 \left[1 + \Delta R\right] \tag{1.3}$$

where $m_{\rho,\omega}$, m_{K^*} and M_B are the masses of the ρ, ω, K^* and B mesons respectively, ζ is the ratio of transition form factors and ΔR parametrizes the remaining small dynamical differences, mainly contributions from annihilation and four-quark operators. Annihilation operator effects are significant for B^+ decays but not B^0 decays, so separating B^+ and B^0 decays can help to understand this contribution. The current constraint on $|V_{td}|/|V_{ts}|$ from $B \to (\rho/\omega)\gamma$ is $|V_{td}|/|V_{ts}| = 0.200^{+0.021}_{-0.020}(\text{sys}) \pm 0.015(\text{stat})$ [4], which is in agreement with the value extracted from B-mixing.

A semi-inclusive analysis was done at *BABAR* where $B \to X_d\gamma$ transitions were considered, resulting in a $|V_{td}|/|V_{ts}|$ average value of $0.199 \pm 0.032(\text{stat}) \pm 0.001(\text{sys})$; this also agrees with the average B-mixing value. Combining this with the constraints from inclusive $(\rho/\omega)\gamma$, we find a value of $|V_{td}|/|V_{ts}|$ of 0.206 ± 0.019 from radiative penguin decays. The current constraints on $|V_{td}|/|V_{ts}|$ from $B \to (\rho/\omega)\gamma$ and $B \to X_d\gamma$ penguin branching fractions and the average B-mixing value are shown in Figure 1.3. As seen in the figure the values found for $|V_{td}|/|V_{ts}|$ in the aforementioned transitions agree with the average B-mixing values, placing a tight constraint on contributions from NP.

1.3.3 TDCPV in Radiative Penguin Decays

Yet another way to investigate the proportions of the $b \to d\gamma$ transition is to look for TDCPV in these radiative penguin transitions. The $B^0 \to \rho^0\gamma$ decays have a time dependence given by Equation 1.4 [17] (described in more detail in Section 3.1.3) containing the aforementioned CP-violation parameters S, the time-dependent asymmetry including mixing, and C, the direct CP-asymmetry.

$$\mathcal{P}_{\pm}(\Delta t) = \frac{1}{4\tau_B} e^{-|\Delta t|/\tau_B} \left[1 \pm S \sin(\Delta m_d \Delta t) \mp C \cos(\Delta m_d \Delta t)\right] \qquad (1.4)$$

The measurement of TDCPV is independent of both the B-mixing and radiative penguin branching fraction measurements and provides an independent constraint of the quark-field parameters as well as possibly uncovering NP signatures.

Signals for $B^0 \to \rho^0\gamma$ have been established by BELLE [2] and *BABAR* [4]. In 2007 the first measurement of the CP-violating parameters S and C in $B^0 \to \rho^0\gamma$ decays was carried out at BELLE. Based on a data sample of 657×10^6 $B\overline{B}$ pairs, S and C were found to be $S_{\rho^0\gamma} = -0.83 \pm 0.65(\text{stat}) \pm 0.18(\text{sys})$ and $C_{\rho^0\gamma} = 0.44 \pm 0.49(\text{stat}) \pm 0.14(\text{sys})$ [6]. This thesis presents progress towards the measurement with the data collected at the *BABAR* detector.

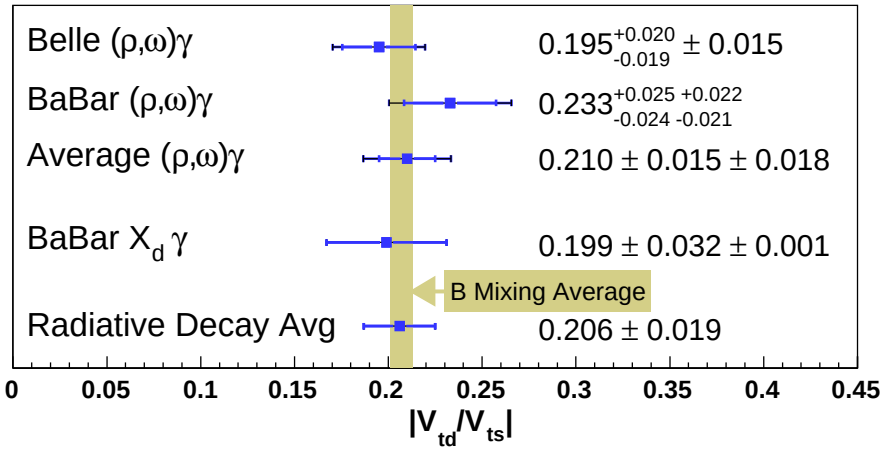

Figure 1.3: Current constraints on $|V_{td}|/|V_{ts}|$ from BELLE and *BABAR*. The B_s and B_d mixing average is represented by the shaded vertical line. The various inclusive and exclusive branching fraction measurements are represented by the blue horizontal lines. The average B-mixing and branching fraction measurements of $|V_{td}|/|V_{ts}|$ agree, placing a tight constraint on contributions from NP.

Chapter 2

The *BABAR* Detector

This analysis was performed using data recorded at the *BABAR* detector at the Stanford Linear Accelerator Center (SLAC). *BABAR* was built to study CP-asymmetry in B meson decays and to test whether the CKM picture of CP-violation in the Standard Model (SM) accounts for observations in the laboratory. *BABAR* was also built to measure rare decays such as the $b \to d\gamma$ transition detailed in this thesis. An accurate reconstruction of the proper lifetime difference between the two B mesons produced by $\Upsilon(4S)$ decays is needed to study the time dependence of the many B decay modes to CP eigenstates in order to determine the CKM angles through TDCPV. For this reason *BABAR* was built in conjunction with the antisymmetric-energy PEP-II storage rings.

The *BABAR* detector recorded 468 fb^{-1} of data at the $\Upsilon(4S)$ resonance from October 1999 through September 2007 (see Figure 2.1), corresponding to 465 million $B\overline{B}$ meson pairs. The large number of B mesons produced by PEP-

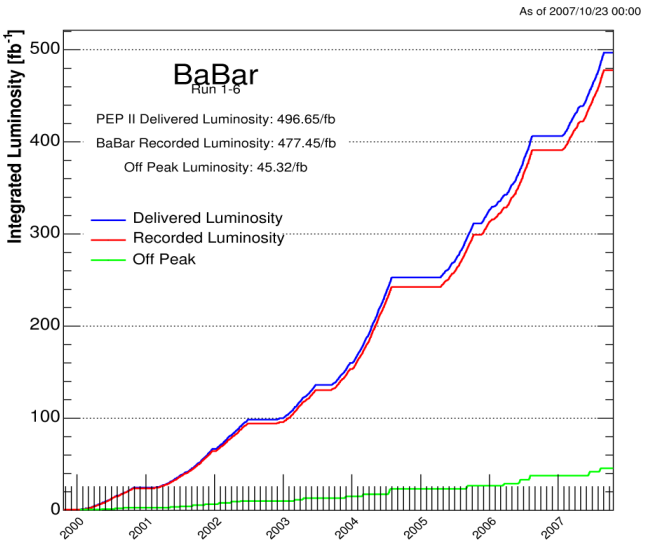

Figure 2.1: Integrated Luminosity recorded at *BABAR* runs 1-6

II allows for the study of rare B decays such as the radiative penguin decays measured in this analysis.

The *BABAR* detector consists of five sub-detectors. The charged-particle tracking system is composed of a five-layer, double-sided silicon strip detector and a 40-layer drift chamber. A ring-imaging Cherenkov light detector determines particle velocities for particle identification. The electromagnetic calorimeter uses 6,580 cesium iodide crystals to determine photon and electron energies. All of these sub-detectors are inside a 1.5T magnetic field produced by a superconducting solenoid pointing along the e^- beam or $+z$ direction along the beam-path at the center of the detector. The outermost steel magnetic flux return system identifies muons and neutral hadrons. A full description of these subsystems can be found in [18].

2.1 Physics at an Asymmetric-Energy Collider

Electron-positron collisions occur in PEP-II at a center-of-mass (CM) energy of 10.58 GeV, corresponding to the $\Upsilon(4S)$ resonance. The $\Upsilon(4S)$ decays nearly exclusively to $B\overline{B}$ meson pairs. The B mesons are produced nearly at rest in the CM frame with momenta of about 340 MeV, leading to a flight length on the order of 30 μm. This distance is too small to measure with current technologies. To get around this, the electron and positron beams collide at asymmetric energies producing a moving $B\overline{B}$ system in the laboratory frame along the axis of the beams. The 9.0 GeV electrons colliding with the 3.1 GeV positrons yield a boost of $\beta\gamma = 0.56$, and larger B decay separations along the z axis in the electron direction. In this configuration, the mean vertex separation Δz is on the order of 250 μm, within the capabilities of the vertex tracker to measure.

The boost in the forward direction leads to differing detector coverage in the laboratory and CM frames. The *BABAR* coordinates are based on a right-handed system such that the $+z$-axis is parallel to the magnetic field of the solenoid and in the direction of the high energy (nominally the electron) beam, the $+y$-axis points vertically upward, and the origin is the nominal interaction point. The conversion of the polar angles, measured from the $+z$ direction, in the two frames is related by

$$cos\theta_{Lab} = \frac{\gamma cos\theta_{CM} + \gamma\beta}{\sqrt{(\gamma cos\theta_{CM} + \gamma\beta)^2 + sin^2\theta_{CM}}}. \tag{2.1}$$

For example, a polar angle of 90° in the CM frame corresponds to about 60° in the laboratory frame. Therefore the *BABAR* detector was designed with more sensitivity and granularity in the forward direction.

2.2 Charged Particle Tracking

The charged particle tracking system is the innermost subsystem of the *BABAR* detector. The tracking system is comprised of a silicon vertex tracker (SVT) and a small-cell drift chamber (DCH) designed to measure the trajectory of a charged particle in a magnetic field in order to deduce the particle's momentum, charge, and distance of closest approach to the interaction point. Measurements of ionization energy loss ($\partial E/\partial x$) provide further information about the identity of the particle.

2.2.1 Silicon Vertex Tracker

The SVT is composed of five layers of double-sided silicon strip detectors and surrounds the interaction point covering a range of polar angles from $\theta = 20^\circ$ to $\theta = 150^\circ$, the first layer being just 4 mm outside the beam pipe and 32 mm from the interaction point. A longitudinal cross section of the SVT is shown in Figure 2.2.

Being the innermost subsystem of the *BABAR* detector, the SVT is responsible for precise spatial and angular measurements of charged-particle trajectories near the interaction point and $\partial E/\partial x$ through charge deposition in the silicon strips. The SVT is the most sensitive part of the *BABAR* tracking system to low transverse momenta; it can measure particles with momenta less than 120 MeV which do not reach the drift chamber. These measurements are crucial in reconstructing B decay vertexes, identifying charged pions to reconstruct ρ^0 candidates and deter-

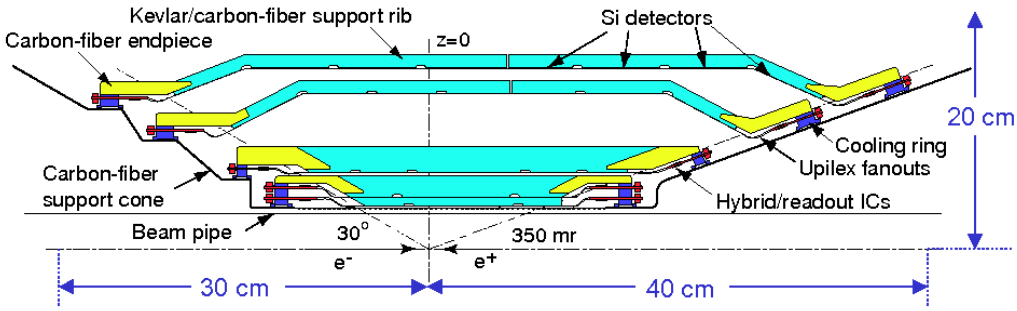

Figure 2.2: Longitudinal cross section of the SVT showing the 5 layers of double-sided, AC-coupled silicon.

mining Cherenkov light angles produced in the particle identification system (see Section 2.2.3).

For normally-incident tracks the three inner SVT layers each have a typical spatial resolution of 15 μm. For the two outer layers the resolution is about 40 μm. The vertex resolution of a fully-reconstructed B meson is 70 μm in the z direction, and better than 100 μm in the $x - y$ plane. The average efficiency for active modules was 92%.

2.2.2 Drift Chamber

The Drift Chamber (DCH) measures charged-particle trajectories and ionization energy loss. Within the magnetic field the charged-particle paths are helices oriented along the field lines, with the radius of curvature determined by the transverse momentum and the dip angle by the ratio of transverse-to-longitudinal momentum.

The DCH has an inner radius of 23.6 cm, just outside of the SVT, and an outer radius of 80.9 cm. An 80:20 mixture of helium and isobutane fills the DCH providing a medium for the charged particles to ionize. Charged particles passing through a cell ionize the gas, those ions in turn drift within the 1,945 V potential across the cell to the closest wire which cross each cell. The 7,104 cells are arranged into 40 layers with each four-layer group of cells associated together as a super-layer. A schematic of the first four super-layers is shown in Figure 2.3. The position resolution ranges from about 100 μm at 5 mm from the each wire to 400 μm at 10 mm.

The drift time measures the location of the particle, while the charge deposited in the gas collected by the sense wire gives information about the particle's energy loss. Particle identification is done using the DCH by comparing the energy loss with the momentum of the particle in question. The typical $\partial E/\partial x$ resolution is approximately 7.5%.

2.2.3 Cherenkov Detector

Particle identification is done complementarily by the DCH and the Detector of Internally Reflected Cherenkov Radiation (DIRC). Particle identification is essential for B^0 flavor tagging, reconstructing rare B decays, and distinguishing between charged pions and kaons. The latter is essential in this analysis since $B \to K^*\gamma$ events comprise a substantial amount of the background. The DCH's ability to distinguish between charged pions and kaons falls sharply for momenta above 700 MeV; however, the information from the DIRC becomes relevant for

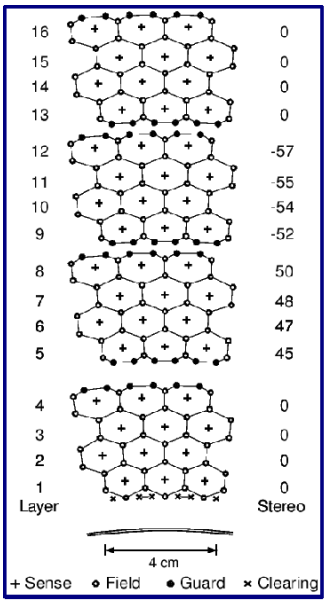

Figure 2.3: Transverse section of the first four super-layers of the DCH.

this range.

The DIRC is designed to measure the Cherenkov radiation angles, θ_C, defined as the angle between the the emitted photons and the direction of the tracks of charged particles moving faster than the speed of light in quartz bars: $\cos\theta_C = 1/(n\beta)$, where $n = 1.473$ is the index of refraction of quartz. The bars are located just outside of the DCH and transport the light through total internal reflection to a reservoir of purified water located on the backward end of the *BABAR* detector. An array of photomultiplier tubes around the reservoir reconstructs the Cherenkov radiation rings and measures the Cherenkov angle θ_C.

The DIRC performance is measured using samples of dimuon events and $D^0 \to K^-\pi^+$ events. In the former, the Cherenkov angle is found to be measured with a precision of 10.2 mrad and a time resolution of 1.7 ns. In the latter sample, kaons

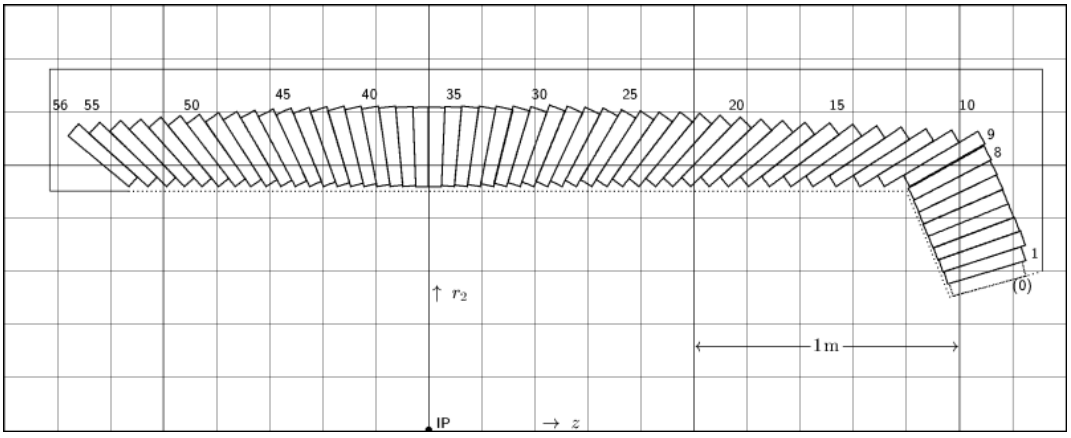

Figure 2.4: Schematic r-z view of the calorimeter, with numbers corresponding to the theta index of the crystal rings.

and pions can be distinguished at the 4.2 σ level at momenta of 3 GeV.

2.3 Electromagnetic Calorimeter

The Electromagnetic Calorimeter (EMC) measures photon energies deposited as electromagnetic showers and discriminates between electrons and other charged tracks. The signature high energy photon of a radiative penguin decay, π^0's, and η's are all reconstructed from photons detected in the EMC.

The EMC is comprised of Thallium-doped CsI crystals arranged in a barrel section with 48 rings of 120 crystals each, starting at an inner radius of 92 cm. The typical crystal face is 4.7 cm^2 and the barrel covers a polar angle down to 15.8° (see Figure 2.4). As photons and electrons with energies above 10 MeV pass through the the material they deposit that energy mainly through pair production and bremsstrahlung radiation in the crystals. These two effects are exploited to

create a detectable cascade of photons – signals used to reconstruct the track and energy of the original particle.

The EMC detects photons ranging in energy from 20 MeV to 9 GeV with an energy resolution of less than $2\%/\sqrt{E}$.

2.4 Muon Detection System

The outermost system of the *BABAR* detector serves to contain the magnetic flux produced by the 1.5 T superconducting solenoid, while acting as a detection system for muons and neutral hadrons. It consists of steel interleaved with resistive plate chambers and limited streamer tubes. This sub-detector system is not utilized in this analysis.

Chapter 3

Analysis Overview

This analysis requires the exclusive reconstruction of the decay mode $f_{\rm rec} = B^0 \to \rho^0\gamma$, where ρ^0 decays to $\pi^+\pi^-$ nearly 100% of the time. Due to the low mass of the particles in the final state and the two-body kinematics the photon and the meson are produced with high momenta in the B rest frame. The high momentum of the photon allows the reduction of the combinatorial background due to π^0 and η decays to two photons. However, the background from continuum events is immense, so developing a dedicated classification tool to suppress these backgrounds is crucial in order to obtain the sensitivity needed – this is done using a Boosted Decision Tree (described in Section 6.1).

In addition to the high levels of continuum backgrounds, signal events also need to be separated from $B\overline{B}$ decays, such as $B \to X_s\gamma$ (mostly $B^0 \to K^{*0}\gamma$), $B^0 \to \omega\gamma$, $B^+ \to \rho^+\gamma$, and $B \to \rho(\pi^0/\eta)$. However these backgrounds are small due to the exclusive reconstruction of $B \to \rho\gamma$ mode, which is fitted with the

kinematic variables ΔE^* and $m_{\rm ES}$ (described below) along with the time difference of the reconstructed ($f_{\rm rec}$) and self-tagged ($f_{\rm tag}$) decays' Δt. The CPV parameters S and C are then extracted from this fit.

This study was performed using *BABAR*'s runs 1-6 data and the internal *BABAR* computing framework 24.3.2 (also known as `analysis-51`). The first set of broad cuts, known as the `BtoRhoGamma` skim, described in more detail in Section 5 and Appendix B of [19], uses the existence of a high energy photon, at least two charged tracks, appropriate meson candidates and event shape variables to initially reduce the data. The second round of reduction cuts, including a cut on the multivariate selector, further separate the signal events from the generic $B\overline{B}$ and continuum backgrounds. This secondary reduction is described in Section 5.4.

Monte Carlo (MC) simulated data were used to validate the performance of the code, perform cut optimization, and develop and validate the fit. The `R24d` skimming cycle was used to generate all data and MC samples. The amounts of generated MC before and after the skim cuts can be found in Table 5.1.

3.1 Kinematic Variables: ΔE^*, $m_{\rm ES}$ and Δt

The primary way to identify B decays over background is to isolate a window around variables whose distributions show a peak for such decays. The commonly used kinematic variables ΔE^* and $m_{\rm ES}$ are used both to define the signal region and, along with Δt, fit the $B^0 \to \rho^0\gamma$ signal and background shapes. First we do a loose fit over large ranges of $m_{\rm ES}$ and ΔE^* to find the expected yields and

define the continuum shape, then, reducing to the signal region in $m_{\rm ES}$, a second fit is done in order to extract the values of the CP-violation parameters S and C (see Equation 1.4).

3.1.1 ΔE^*

ΔE^* is the energy difference between the beam and the reconstructed B-meson:

$$\Delta E^* = E^*_\gamma + E^*_{had} - E^*_{beam} \tag{3.1}$$

In this equation, a "$*$" indicates a center-of-mass quantity. E^*_γ is the high energy photon energy, E^*_{had} is the total hadronic energy of the decay, and E^*_{beam} is the per-particle CM energy of either beam. For correctly reconstructed events ΔE^* peaks near zero. Mis-reconstructed B mesons will in general exhibit a peaking shape that is shifted due to a missed or misidentified particle.

3.1.2 $m_{\rm ES}$

The beam-constrained mass, or $m_{\rm ES}$, defined as

$$m_{\rm ES} = \sqrt{E^{*2}_{beam} - p^{*2}_B} \tag{3.2}$$

is the second kinematic variable used to define the signal region and carry out the fit. The quantity p^*_B is the B momentum in the CM frame and is calculated using a photon momentum scaled such that $\Delta E^* = 0$. By rescaling the photon

momentum, we eliminate dependence on the calorimeter resolution which would otherwise create an asymmetry in the signal distribution. Instead the resolution of $m_{\rm ES}$ is determined by the beam energy spread. True signal events peak at the B mass of 5.278 GeV. Mis-reconstructed B mesons can also peak in $m_{\rm ES}$ while other backgrounds appear flat.

3.1.3 Δt

Once produced, the $B\overline{B}$ mesons travel down the beam-pipe in the lab-frame and decay independently. One of the mesons decays into a final state $f_{\rm tag}$, establishing its flavor at the time of decay, while the other meson is reconstructed as signal. The signal B mesons decay at time $t_{\rm rec}$ to a final state $f_{\rm rec}$ and the tagged mesons decay at time $t_{\rm tag}$ to a final state $f_{\rm tag}$. The time difference $t_{\rm rec} - t_{\rm tag}$ is defined as Δt. Since the B^0 and $\bar{B}^0$ mesons are approximately at rest in the $\Upsilon(4S)$ CM, Δt can be determined from the displacement in z between the $f_{\rm rec}$ and $f_{\rm tag}$ decay vertexes:

$$\Delta t \simeq \frac{(z_{\rm rec} - z_{\rm tag})}{\beta\gamma c} \equiv \frac{\Delta z}{\beta\gamma c}.$$

The Δz information collected in the SVT is used to calculate the time difference, Δt, between the tagging and signal decay.

The e^+e^- collisions are tuned to the resonant $\Upsilon(4S)$ energy of 10.58 GeV. The $\Upsilon(4S)$ mesons are produced with a Lorentz boost of $\beta\gamma = 0.56$ in the center of the *BABAR* detector within the SVT. The decay chain $\Upsilon(4S) \to B^0\bar{B}^0 \to f_{\rm rec}f_{\rm tag}$ has a time dependence given by Equation 1.4, reproduced here:

$$\mathcal{P}_{\pm}(\Delta t) = \frac{1}{4\tau_B} e^{-|\Delta t|/\tau_B} \left[1 \pm S \sin(\Delta m \Delta t) \mp C \cos(\Delta m \Delta t)\right]$$

The above probability distribution describes a final state with one CP eigenstate and one self-tagging state which determines the B flavor at the time of decay. Here τ_B is the B^0 lifetime, Δm is the mass difference between the two B^0 mass eigenstates, Δt is the time difference $(t_{\rm rec} - t_{\rm tag})$, and the subscript $\pm$ refers to the b-flavor charge: $\mathcal{P}_+$ when the tagging B meson is a B^0 and $\mathcal{P}_-$ for $\bar{B}^0$. Finally, S and C are the TDCPV parameters. S is a measure of CP-violation due to interference between B^0 decays with and without mixing. C is determined by the direct CP-asymmetry A_{CP};

$$C = -A_{CP} = \frac{\mathcal{B}(B^0) - \mathcal{B}(\bar{B}^0)}{\mathcal{B}(B^0) + \mathcal{B}(\bar{B}^0)}.$$

The SM predicts no time-dependent CP-asymmetry due to interference between B^0 decays with and without mixing ($S = 0$) and 10% for the direct CP-asymmetry (C) for $B^0 \to \rho^0\gamma$ [20][21]. The SM also restricts the range of the parameter C relative to S by

$$S^2 + C^2 \leq 1$$

[17].

The strategy for this analysis is to use the Δz information to estimate Δt and then perform a maximum likelihood fit to the data using the above probability distribution within the signal region defined by the kinematic variables ΔE^* and $m_{\rm ES}$. The CP-violating parameters S and C are then extracted from this fit.

Chapter 4

Background Summary

Since the $B^0 \to \rho^0\gamma$ branching fraction is $\mathcal{O}(10^{-6})$, care must be taken to suppress and account for the various backgrounds. The majority of these background events consist of $e^+e^- \to q\overline{q}$, where $q\overline{q}$ are light quark pairs. There are also significant expected $B\overline{B}$ backgrounds that generally display a peaking shape in $m_{\rm ES}$ and a peak offset from zero, or, no peak at all in ΔE^*. The $m_{\rm ES}$, ΔE^*, and Δt MC distributions are shown in Figures 7.1 through 7.12 in Section 7.1.

4.1 Continuum

Light quark pairs from $e^+e^- \to u\overline{u}$, $d\overline{d}$, $c\overline{c}$, $s\overline{s}$, and $\tau^+\tau^-$ events constitute the largest background source and are referred to collectively as continuum. Continuum decays can be mis-reconstructed as signal when they contain a high energy photon. There are two primary processes that lead to this condition: Initial State

Radiation (ISR) and a highly asymmetric π^0/η decay.

In ISR decays, the high energy photon emitted by the beam electron or positron causes a boost in the CM frame of the collision relative to the expected standard CM, resulting in a back-to-back two-jet topology in the frame recoiling from the photon. The jet-like topology of the light quark pair productions is contrasted with the signal $B^0 \to \rho^0\gamma$ event's isotropic shape. To exploit this difference, quantities that characterize the distribution of activity over the entire event are fed into a decision tree-based neural simulator which outputs a single categorization variable separating continuum background from signal $B^0 \to \rho^0\gamma$ decays. The multivariate decision tree and selection variables are described in Section 5.

4.2 $B\overline{B}$

The $B\overline{B}$ decays are first divided into B^+B^- or $B^0\bar{B}^0$ decays, then they are split according to whether they are $B^+ \to \rho^+\gamma$, $B^0 \to \omega\gamma$, $B \to K^*\gamma$ events or other generic B decays. The remaining sample contains both inclusive B meson decays as well as $b \to d\gamma$ and $b \to s\gamma$ transitions for which the hadronic final state is not composed of one of the specific resonances.

4.2.1 $B^+ \to \rho^+\gamma$ and $B^0 \to \omega\gamma$

Fortunately these backgrounds are considerably smaller than the generic B or K^* backgrounds and can simply be subtracted off of the signal peak shape. The $B^+ \to \rho^+\gamma$ has an offset peak in ΔE^* and no peak in $m_{\rm ES}$, the $B^0 \to \omega\gamma$ peaks

around 0 in ΔE^* and around the B mass in $m_{\rm ES}$. As a result they are incorporated into the first peaking cocktail fitting category described in Section 8.6.

4.2.2 $B \to K^*\gamma$

The $B \to K^*\gamma$ events most likely to be mis-identified as signal $B^0 \to \rho^0\gamma$ are the following:

- $B^0 \to K^{*0}\gamma$, $K^{*0} \to K^+\pi^-$
- $B^0 \to K^{*0}\gamma$, $K^{*0} \to K^0_s\pi^0$
- $B^\pm \to K^{*\pm}\gamma$, $K^{*\pm} \to K^\pm\pi^0$
- $B^\pm \to K^{*\pm}\gamma$, $K^{*\pm} \to K^0_s\pi^\pm$

The first is the only mode above that displays a peak in $m_{\rm ES}$ while all modes have a peak shifted from zero in ΔE^*. The $K^+\pi^-$ and $K^0_s\pi^\pm$ modes contribute a considerable amount of background events. The events with a charged pion in the final state contribute a sizable background while the events with a π^0 in the final state are negligible. The shift from zero in the ΔE^* peak is exploited in the fitting procedure and used to subtract these backgrounds.

4.2.3 Generic B

Since actual B mesons are also the source of these backgrounds, generic B decays share the isotropic shape of the signal and can peak in our kinematic

discriminators ΔE^* and $m_{\rm ES}$. Decays that simultaneously peak in ΔE^* and $m_{\rm ES}$ are usually the result of a highly asymmetric π^0 or η decay originating from $b \to d\pi^0$ or $b \to d\eta$ in which the lower energy photon from the $\pi^0/\eta \to \gamma\gamma$ is missed in the reconstruction.

Again, the shift from zero in the ΔE^* peak is exploited in the fitting procedure and used to subtract these generic B backgrounds.

4.3 Blind Analysis

Analyses performed at *BABAR* are blind which means that the event selection is based on simulated data rather than the actual data collected in the *BABAR* detector. The *BABAR* Simulation Group has developed software that simulates the environment of the *BABAR* detector and its effect on particle decays consisting of two main components [22]: EvtGen and GEANT4. EvtGen generates events based on quantum amplitudes for specific decays, allowing for the possibility of interference [23] – critical for simulating the time-dependence of B^0 mixing and decay, and angular distributions of final-state particles based on helicity amplitudes. After long-lived particles have been produced, they are passed through a detailed GEANT4 simulation of the detector material, simulating processes like bremsstrahlung, multiple scattering, photon conversion and decays of long-lived particles such as pions [24].

The actual data is not processed until all of the event selection decisions are in place and the fitting strategy is set, preventing a bias in the results.

4.3.1 Monte Carlo Samples

The generic $B\overline{B}$ and continuum MC samples produced for optimization of selection criteria and for analysis technique validation are summarized in Table 4.1 and the $B \to K^*\gamma$ and $B^0 \to \rho^0\gamma$ signal MC samples are summarized in Table 4.2. These MC samples were skimmed using the `R24a3` skim cycle which is described in Section 5.1. Statistics are limited by the availability of the *uds* and (less importantly) τ generic samples. For this reason the data itself will be used to determine the size of the continuum background, via the fitting procedure that will be described in Chapter 8.

Run	$B^0\bar{B}^0$	B^+B^-	$c\overline{c}$	uds	τ
1	35M	26M	55M	45M	20M
2	104M	103M	164M	133M	57M
3	58M	50M	88M	71M	29M
4	170M	267M	253M	217M	95M
5	216M	331M	367M	257M	119M
6	135M	209M	157M	167M	73M
Total	718M	1114M	1088M	889M	393M
Luminosity in fb^{-1}:	1301.06	1350.02	857.24	425.44	417.96

Table 4.1: Summary of $B^0 \to \rho^0\gamma$ background MC data sets for runs 1-6 in the `R24a3` skim cycle.

Mode	**Signal**
$B^+ \to \rho^+\gamma$	650K
$B^0 \to \rho^0\gamma$	650K
$B^0 \to \omega\gamma$	650K
$K^{*0} \to K^+\pi^-$	2149K
$K^{*+} \to K^+\pi^0$	2149K
$K^{*+} \to K_s^0\pi^+$	2149K
$K^{*0} \to K_s^0\pi^0$	650K

Table 4.2: Summary of $B^0 \to \rho^0\gamma$, $B^+ \to \rho^+\gamma$, $B^0 \to \omega\gamma$, and $B \to K^*\gamma$ MC data sets for runs 1-6 in the `R24a3` skim cycle

Chapter 5

Candidate Selection

Before the CP-asymmetry parameters can be investigated the proper decay must first be reconstructed: $B^0 \to \rho^0\gamma$ with $\rho^0 \to \pi^+\pi^-$, the latter happening essentially one hundred percent of the time. A common template for *BABAR* analyses is adhered to in this study where the event reconstruction happens in several distinct stages.

The first stage is a set of cuts run over all of the decays reconstructed in the *BABAR* detector. These cuts are designed to eliminate the vast majority of unwanted events discarding those that do not satisfy minimal criteria. These cuts are generally referred to as a "skim" and are essential since they reduce the several terabytes of data to a more manageable size.

Next, a full picture of the decay is pieced together. Using centralized software routines particles are reconstructed from primary event information collected in the detector. These particles are are then used to combine individual candidates

into composites. In our case we combine charged pions into a ρ^0; the resulting meson is then combined with the high energy photon to form the signal B candidate. The accompanying B meson is then flavor tagged. At all stages we require that the daughter particles originate from the same point (based on kinematic fits and geometric constraints) and that the mass of the resulting parent is consistent with the currently accepted value.

Finally, various event shape quantities are computed and saved for the reconstructed events, including spatial distributions of the decay products and angular relationships between individual (or groups of) particles. It is important to note that multiple reconstructions are possible for the same event, in which case we save all the possibilities and decide which particular one to choose at a later stage of the analysis.

Separating the $B^0 \to \rho^0\gamma$ signal from the background events is paramount in this analysis. It is possible to mis-reconstruct a kaon as a pion, allowing $B \to K^*\gamma$ backgrounds to leak in, or to use a photon originating from a π^0 or η decay as the primary photon candidate after losing the other photon during reconstruction. Since the π^0 and η are light mesons they are produced copiously in the continuum (the majority of decays that do not proceed through the $\Upsilon(4S)$).

Due to the two-body kinematics and the low mass of the particles in the final state, the photon and the meson are produced with relatively high momentum in the B reference frame. The high momentum of this signal photon allows reduction of the combinatorial background due to π^0 and η decays. Nevertheless, the background from the continuum is overwhelming, and developing a dedicated

classification tool for continuum suppression is crucial to achieve the sensitivity needed for the measurement. A Bagged Decision Tree, described in Section 6, was used to carry out this classification and separation while minimizing the error on the CP-asymmetry parameter S.

5.1 Skim Selection

This analysis uses the `BtoRhoGamma R24a3` skim in *BABAR*'s `FilterTools` package, which contains the skims for all *BABAR* analyses. Events passing this particular skim must satisfy the following conditions:

- The event passes either the `BGFMultiHadron` (at least three charged tracks have been identified in the event) or the `BGFNeutralHadron` (selects photons with c.m.s. momentum > 500MeV and $-0.75 < \cos(\theta_\gamma) < 0.96$) tag filter.
- There are at least two tracks in the `GoodTracksLoose` list, which requires tracks to have at least 100 MeV of transverse momentum, with maximum momentum of 10 GeV, at least 12 hits recorded in the drift chamber, and imposes basic restrictions on the point of closest approach to the interaction point.
- Event shape: ratio of the 2^{nd} and 0^{th} Fox–Wolfram moments [25] (R_2^{All})< 0.9, where $R_l = \sum_{i,j} \frac{p_i^* p_j^*}{s} P_l(cos\theta_{ij}^*)$. Here, P_l is the l-th order Legendre polynomial and the sum involves particles of c.m.s. momenta p_i^* and p_j^*, separated by an angle θ_{ij}^*.

- The primary photon CM energy is in the range [1.5, 3.5] GeV.
- The meson candidate mass is in the range [0.5, 1.2] GeV, [0.5, 1.3] GeV, and within 0.05 GeV around the nominal ω mass for the ρ^0, ρ^+ and ω modes, respectively (historically the `BtoRhoGamma` skim includes the ρ^+ and ω modes).
- Loose kinematic cuts: $5.1 < m_{\rm ES} < 5.5$ GeV and $-0.6 < \Delta E < 0.6$ GeV.
- The trajectories of the ρ^0 daughters are compatible with a common vertex.

Skim efficiencies for MC generated events are listed in Table 5.1. Further processing of the events, including the full candidate reconstruction described earlier, calculating various event and candidate-level quantities, and further selection cuts (to be described below) are applied to this reduced data set. The reduction efficiencies are listed in Table 5.2.

5.2 Charged Pion Selection

Since it is so important that the pions from a ρ^0 decay are correctly identified, a dedicated pion selector, based on centralized software routines, is invoked.

Misidentifying kaons as pions allows $B \to K^*\gamma$ background to leak though into our signal region. The optimum selection, based on *BABAR*'s standard particle identification algorithms, was determined via a detailed study in the runs 1-4 analysis (documented in [26], Section 3.4). *BABAR* uses various classification techniques, such as likelihood ratios and artificial neural networks, to correctly identify

data set	**pre-skim**	**post-skim**	ϵ[%]
$B^0\bar{B}^0$	717995000	321736	0.0448
B^+B^-	708762000	432650	0.0611
$c\overline{c}$	1114408000	16962318	1.52
uds	889163000	35283007	3.97
τ	392887000	4975250	1.27
$\rho^0\gamma$	650000	469172	72.2

Table 5.1: `BtoRhoGamma R24a3` skim MC skim efficiencies. Efficiencies are not relative to the preceding step.

data set	**pre-reduction**	**post-reduction**	ϵ[%]
$B^0\bar{B}^0$	321736	787	0.24
B^+B^-	432650	968	0.22
$c\overline{c}$	16962318	28690	0.17
uds	35283007	98166	0.28
τ	4975250	4119	0.08
$\rho^0\gamma$	469172	157731	33.6

Table 5.2: `BtoRhoGamma R24a3` Monte Carlo reduction efficiencies. Efficiencies are not relative to the preceding step.

particles based on their attributes and place them into corresponding lists. There is a progression of selector algorithms with increasingly stringent selection criteria, which always introduce the mutually exclusive choice of better background rejection verses higher signal efficiency. These are labeled from `VeryLoose` to `VeryTight` in the *BABAR* software.

The best pion selector for the $B \to \rho\gamma$ modes was found in the most recent *BABAR* branching fraction analysis to be the `piLHVeryTight` [27], combined with a minimal significance criteria of 0.001 on the Poisson probability of the number of the photons seen in the DIRC for a particular candidate being different from the expected number for the assigned pion hypothesis.

5.3 Flavor Tagging

Determining the flavor of a B^0 meson in the event is crucial to TDCPV measurements, this is accomplished at *BABAR* by exploiting correlations between the charges of final-state particles and the flavor of the original B^0 or $\bar{B}^0$ meson.

There are a total of six categories, each with a different level of performance known as Lepton, Kaon 1, Kaon 2, Pion, Kaon-Pion, and Other. There is a seventh category for when no flavor tag can be determined. The categories are characterized by their average efficiencies ϵ, mis-tag probability w, and the flavor differences:

$$\Delta\epsilon = \epsilon_{B^0} - \epsilon_{\bar{B}^0}, \Delta w = w_{B^0} - w_{\bar{B}^0}, \text{ and } \mu \equiv \frac{\epsilon_{B^0} - \epsilon_{\bar{B}^0}}{\epsilon_{B^0} + \epsilon_{\bar{B}^0}}.$$

These values have been cataloged by the B Tagging Group and are displayed in Table 5.3.

5.4 Reduction Cuts

Table 5.4 summarizes the fixed cuts applied after the skim and initial candidate reconstruction but before the multivariate selector optimization is carried out. Included are six pre-cuts on photon quality, which are simultaneously optimized using the Bump Hunter algorithm [28]. The photon quality pre-cuts are meant to clean up the input to the Decision Tree, reducing the size of the training sample and thus making its job much easier, as well as to simplify the estimation of systematic errors later on by cutting away regions of poor agreement between data and simulated events. The reduction variables are as follows (cut values listed in Table 5.4 and reduction efficiencies in Table 5.2):

- `GammaECal` : lab frame-calibrated energy of the EMC cluster
- `Gammas9s25` : ratio of the sums of the energies of the central 9 EMC crystals to the central 25 crystals surrounding the centroid
- `GammaLat` : lateral moment of the EMC cluster
- `GammasecMom` : second moment of the EMC cluster
- `GammaZ20` : absolute value of the complex Zernike(2,0) moment of the EMC cluster

	BFlav MC
$\omega^{\rm signal}$ – Lepton	0.0237 ± 0.0005
$\omega^{\rm signal}$ – Kaon1	0.0549 ± 0.0006
$\omega^{\rm signal}$ – Kaon2	0.1511 ± 0.0006
$\omega^{\rm signal}$ – KaonPion	0.2460 ± 0.0008
$\omega^{\rm signal}$ – Pions	0.3454 ± 0.0007
$\omega^{\rm signal}$ – Other	0.4242 ± 0.0010
$\Delta\omega^{\rm signal}$ – Lepton	-0.0008 ± 0.0009
$\Delta\omega^{\rm signal}$ – Kaon1	0.0018 ± 0.0011
$\Delta\omega^{\rm signal}$ – Kaon2	0.0019 ± 0.0011
$\Delta\omega^{\rm signal}$ – KaonPion	-0.0042 ± 0.0013
$\Delta\omega^{\rm signal}$ – Pions	-0.0222 ± 0.0012
$\Delta\omega^{\rm signal}$ – Other	0.0549 ± 0.0015
$\delta(\Delta t)$(core, signal)−Lepton	-0.0504 ± 0.0051
$\delta(\Delta t)$(core, signal)−Nonlepton	-0.2408 ± 0.0023
Scale(core, signal)−Lepton	1.0106 ± 0.0081
Scale(core, signal)−Nonlepton	1.1033 ± 0.0039
$f_{\rm core,signal}$	0.8937 ± 0.0016
$f_{\rm outlier}$	0.0042 ± 0.0001
$\delta(\Delta t)$(tail)	-1.2558 ± 0.0260
$\epsilon^{\rm signal}_{\rm ratio}$ – Lepton	0.0005 ± 0.0019
$\epsilon^{\rm signal}_{\rm ratio}$ – Kaon1	0.0033 ± 0.0019
$\epsilon^{\rm signal}_{\rm ratio}$ – Kaon2	-0.0008 ± 0.0018
$\epsilon^{\rm signal}_{\rm ratio}$ – KaonPion	0.0041 ± 0.0020
$\epsilon^{\rm signal}_{\rm ratio}$ – Pions	0.0061 ± 0.0018
$\epsilon^{\rm signal}_{\rm ratio}$ – Other	-0.0061 ± 0.0022
$\epsilon^{\rm flav}_{\rm ratio}$	0.0075 ± 0.0009

Table 5.3: `Tag08` Parameters from the B Tagging Group calculated using runs 1-6 MC B-Flavor samples.

Description	$B^0 \to \rho^0\gamma$ mode
high-energy γ	$-0.74 < \cos(\theta) < 0.93$ $n_{\text{crystals}} > 4$ No problem crystal $> 25\,\text{cm}$ isolation
Tracking	GTL requirement for all charged tracks
PID	veryTight π ID + DIRC photon consistency
`R2All`	< 0.7
Converted γ veto	$0.1 \leq m_{\pi^0}^{conv} \leq 0.16$ and $0.5 \leq m_{\eta}^{conv} \leq 0.59$ (GeV^2)
`GammaZ20`	> 0.82
`Gammas9s25`	$[0.93, 0.99]$
`GammaLat`	$[0.12, 0.51]$
`GammaA42`	< 0.08
`GammasecMom`	< 0.002
`GammaECal`	$[1.5, 4.4]$

Table 5.4: Reduction cuts applied after the skim and before optimization is carried out for the remaining criteria.

- `GammaA42` : absolute value of the complex Zernike(4,2) moment of the EMC cluster

5.4.1 Combined Candidate Selection

When there are multiple $B^0 \to \rho^0\gamma$ candidates the final selection chooses the best B meson candidate. As in the previous branching fraction analyses, such candidates are chosen so that the mass of the ρ^0 is closest to the nominal mass – this happens after the reduction cuts.

The final signal efficiencies for the entire candidate selection process (*i.e.* the candidates that pass all cuts and end up in the final fit) are 24% for $B^0 \to \rho^0\gamma$.

For comparison, the corresponding *uds* continuum efficiencies are 0.011%. This is before the multivariate classifier, used to identify continuum events and described in Section 6, is applied.

5.5 Multivariate Optimization

In addition to the selection described so far, several variables are combined in a classification algorithm based on Decision Trees. The classifier output is used to further separate the signal from *udsc* continuum background and to minimize the error on the measured CP-asymmetry parameter S. This final selection algorithm is described in Chapter 6; its optimization is presented in Section 6.4.

Chapter 6

Classification

Multivariate selectors, such as Decision Trees, are effective tools for separating the desired signal from the very large continuum *udsc* backgrounds. Using the `C++`-based package `StatPatternRecogition` [29] this analysis implemented a Bagged Decision Tree (BDT) largely adopted from the most recent $B \to (\rho/\omega)\gamma$ branching fraction measurement [4]. The multivariate selector was trained with the twelve most effective event variables which did not involve the B meson tagging or flight-length information, both of which are input parameters to our likelihood fit discussed in Chapter 8. After training, step-by-step cuts on the BDT output were applied and, for each cut, pure toy studies were performed. The BDT cut that produced the smallest uncertainty on the CP-asymmetry parameter S was used in the final analysis of the data.

6.1 Bagged Decision Trees

A Decision Tree (DT) is a well-known tool in Machine Learning and Data Mining. They are widely used in many fields to identify specific traits in a large sample, such as separating signal from background. DTs consist of decision splits on input variables, referred to as nodes, which terminate at a terminal or leaf node. Each node represents a split on an input variable from the original data-set. Nodes that have child nodes are called interior nodes. In high energy physics, a DT is built by choosing the most useful event variables and making decision splits based on their values.

Generally, the DT creates a model that predicts the value of a target variable based on input variables. This is done by recursive partitioning of subsets, based on an attribute value test, where each node in the tree evaluates an attribute in the data derived from the source set of input variables, and determines which path it should follow. In `StatPatternRecognition`, a decision tree is built by trying all possible splits on all possible variables and choosing the one that optimizes a given figure of merit (FOM). This is done for each new tree node, which is similar to repeatedly making a cut on a kinematic variable for each internal node. Since a single tree cannot contend with the more sophisticated Neural Networks the capabilities of tree-based algorithms are enhanced by applying the modern statistical tool Bootstrap Aggregation.

The idea of Bootstrap Aggregating, or Bagging, is to use bootstrap replicas of data, *i.e.* re-sampling the data a certain number of times, each time selecting, with replacement, a subset of training events. By "averaging" over the bootstrap

samples one gains better accuracy than a single-tree approach. Bootstrap was originally introduced as a way to estimate certain parameters of a statistical distribution, such as correlations among variables, for which there is no closed-form algebraic expression. In the case of DTs, it's a different way of producing a more accurate decision based on a collective vote. The user should make on the order of 100 trees (we used 80 in this study) with a large number of terminal nodes (1,000 in this study) to pick up on the variation among the bootstrap replicas of training data.

6.2 Training Variables

The previous $B \to (\rho/\omega)\gamma$ branching fraction measurement did an extensive study of various multivariate selectors including BDTs [27]. The performance of each multivariate selection process for separating the $B \to (\rho/\omega)\gamma$ signal from the continuum backgrounds was compared. The BDT had the best performance for the $B^0 \to \rho^0\gamma$ mode and has hence been adopted for this analysis.

In this analysis, we considered the sixteen most influential variables from the branching fraction study, documented in [27], to train the BDT. We omitted the variables BKaonValueMor (Kaon based B tag), BdeltaZFitOverErr (Δz, the displacement between the two B vertexes in the z direction, divided by the error), BzCP (the z-component of the decay vertex of the signal B), and BzTag (the z-component of the decay vertex of the tag B) in order to avoid biasing the fitting procedure, which uses tagging information to separate B^0 from $\bar{B}^0$ decays.

The input variables used in this study are as follows:

- `R2All` : The ratio of the 2^{nd} to 0^{th} Fox-Wolfram moments for the event, using `ChargedTracksAcc` and `GoodNeutralLooseAcc` (see Section 5.1).
- `BcosThetaCM` : Cosine of the polar angle of the CM momentum of the signal B.
- `BroeGamL3` : The third normalized Legendre moment, L_3, of the rest of the event (ROE) boosted into the CM frame with respect to the ROE thrust axis. The Legendre moments are given by $L_i = \sum_j \left|p_j^*\right| \left|\cos\theta_j^*\right|^i$, where p_j^* is the CM momentum of each particle j not used to reconstruct the signal B candidate and θ_j^* is the angle between that particle and the thrust axis of the signal B candidate.
- `Rho0helicityAngle` : The angle between the π^+ π^- plane and the B flight direction, both in the ρ^0 rest frame.
- `BRoeMissMass` : Missing mass in the rest of the event (ROE), defined as the set of tracks and calorimeter clusters not associated with the tagged B.
- `GammabestEtaLR` : Likelihood-based veto for $\eta \to \gamma\gamma$ events.
- `BRoePerpPBeam` : Rest of event momentum perpendicular to the beam direction.
- `GammabestPi0LR` : Likelihood-based veto for $\pi \to \gamma\gamma$ events.
- `Rho0chi2Prob` : Probability of the χ^2 with the degree of freedom of the $\rho^0 \to \pi^+\pi^-$ vertex fit.

- `BrecoilR2prime50` : `R2` (see Section 5.1) of EMC bumps of energy greater than 50 MeV in the γ recoil system.
- `Rho0costhCM` : Cosine of the polar angle of the CM momentum of the ρ^0.
- `BRoePlanarity` : A measure of how flat, plane-like, or planar, is the ROE.

6.3 Multivariate Classifier Training

The training of a multivariate classifier is carried out in the following way. Applying all pre-selection criteria (skim and reduction), signal and background Monte Carlo samples are produced. The samples are then split randomly in half, into training and testing subsets. The training algorithm is fed a vector of values corresponding to each input variable for each candidate in the sample. The list of BDT input variables used in this analysis, sorted by their contribution to the overall classifier performance, based on the number of decision splits, is shown in Table 6.1.

Once the classification is complete, it is applied to the testing sample, and the validation curve is plotted (*e.g.* see Figure 6.1). From this curve, one can see whether the training has converged (*i.e.* the loss function has leveled off), or if more cycles are needed (*i.e.* build more trees). If the loss function starts turning back up, for example, the BDT has been over-trained and needs fewer cycles. The validation curve shows that most of the work is done in approximately the first 80 cycles and that each additional cycle after about 100 provides only a small incremental contribution. In this analysis 80 cycles and 1,000 nodes were used.

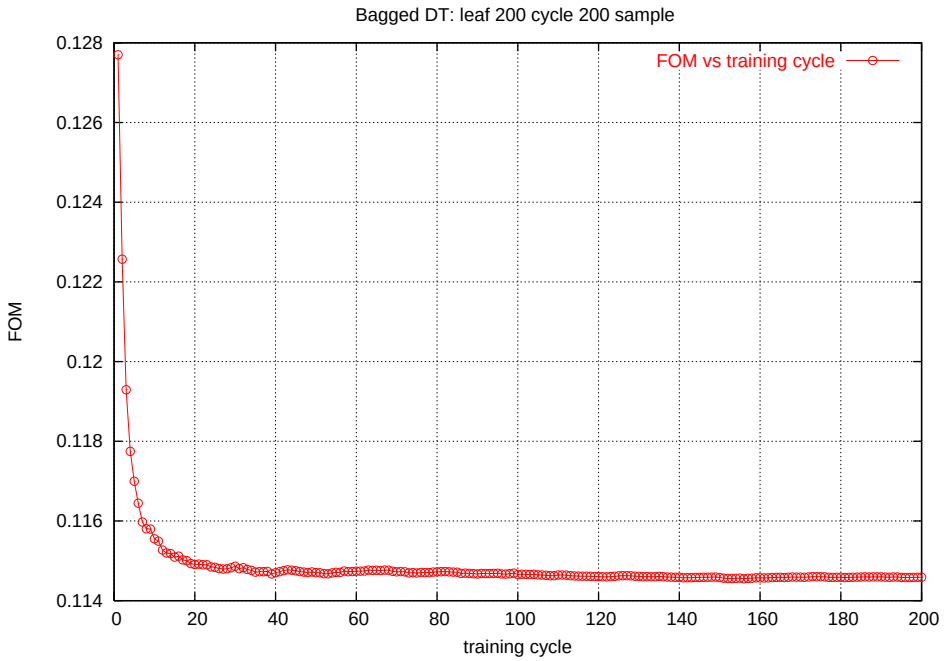

Figure 6.1: Bagger validation curve as a function of training cycle (number of trees). The FOM is the quadratic loss function which measures the difference between the target and the result of the classification, defined as: $(y - f(x))^2$. For example, a signal event with a classifier output of 0.5 corresponds to a loss of $(1 - 0.5)^2 = 0.25$.

The classification output is a value between 0 and 1; 0 for continuum background and 1 for signal. The BDT output trained with these parameters on signal and background continuum MC overlaid with the testing MC samples are shown in Figure 6.2. The background rejection as a function of signal purity curve is shown in Figure 6.3.

Variable	Number of DT Splits
Rho0helicityAngle	49880
BroeGamL3	46997
BcosThetaCM	45090
BRoePerpPBeam	39565
BRoeMissMass	36644
GammabestPi0LR	34792
BrecoilR2prime50	32405
R2All	31617
Rho0costhCM	30225
GammabestEtaLR	25771
Rho0chi2Prob	23236
BRoePlanarity	22214

Table 6.1: Number of DT splits per BDT input variable.

6.4 BDT Output Cut Optimization

After the cycle and node parameters are chosen the next step is to choose the optimal cut on the BDT output. To do this, cuts on the BDT were done in steps of 0.1 from 0.3 to 0.9 and for each cut 1,000 pure toy studies were fitted. Some results of these toy studies are shown in Figures 6.4 and 6.5. The optimal cut at 0.6 was chosen by minimizing the uncertainty on the CP-violation parameter S as a function of the BDT cut. The curve of the BDT cut versus the uncertainty on S is shown in Figure 6.6 and displays a clear minimum at the BDT cut value of 0.6. A cut at this value of the BDT output rejects 88% of the continuum background while preserving 79% of the signal.

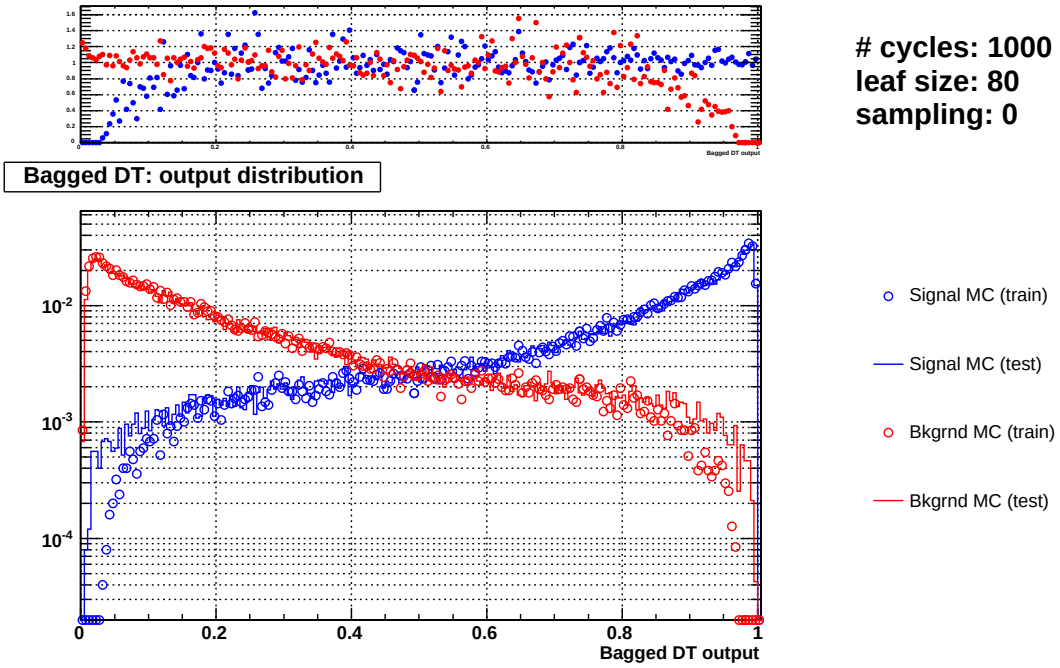

Figure 6.2: Top: Ratio of the trained and tested BDT outputs. Bottom: BDT output distribution for both sub-sets of trained and untrained data.

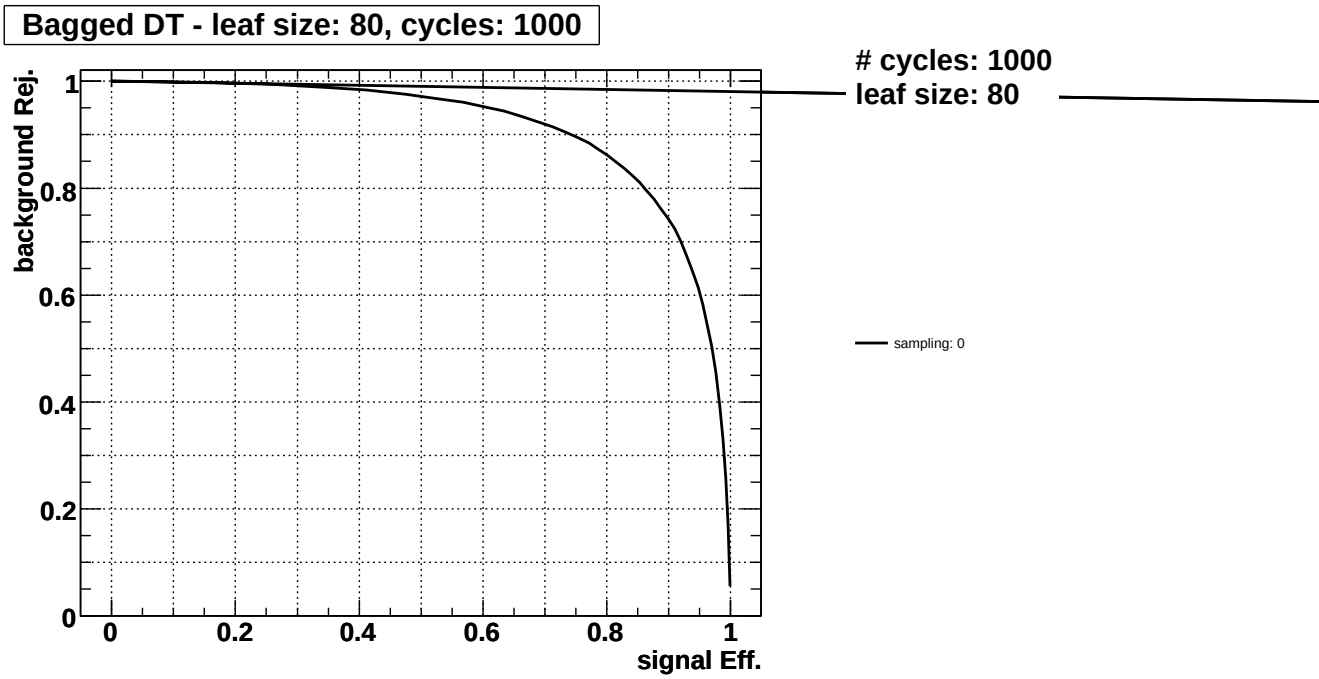

Figure 6.3: Efficiency versus purity distribution for the BDT output. Only continuum background MC used for training.

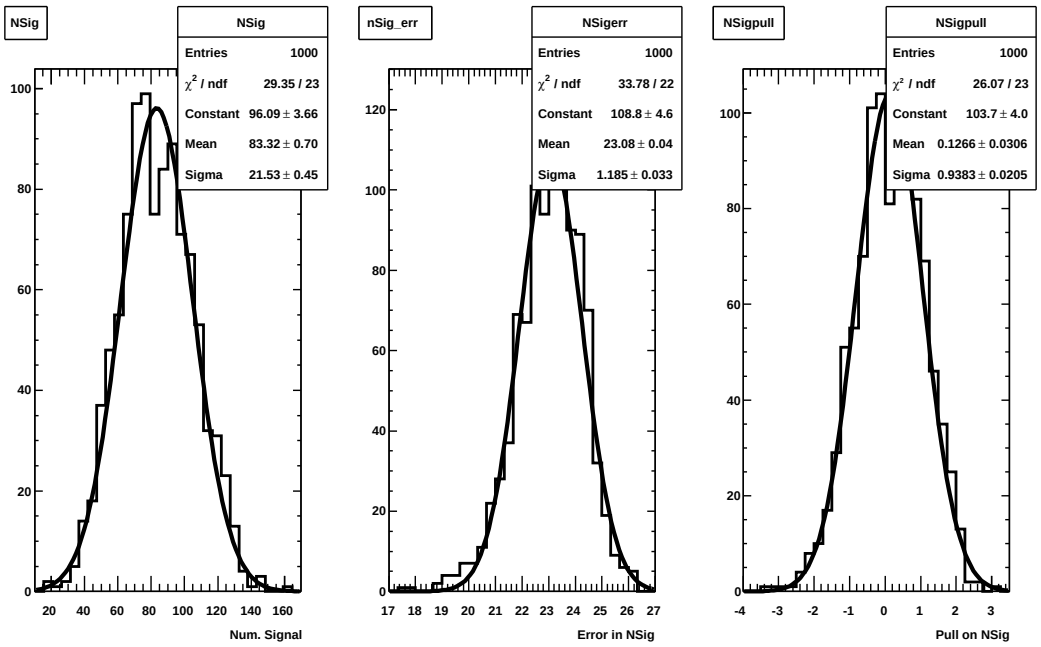

Figure 6.4: Results of fitting 1,000 pure toy studies in the first stage of the maximum likelihood fit (the fit and multistage structure is described in Chapter 8). The plots show the expected number of signal events going into the second stage of the fit and were produced using a cut on the BDT at 0.6. This cut resulted in the smallest uncertainty for the CP-violation parameter S and was used in the final fit to data.

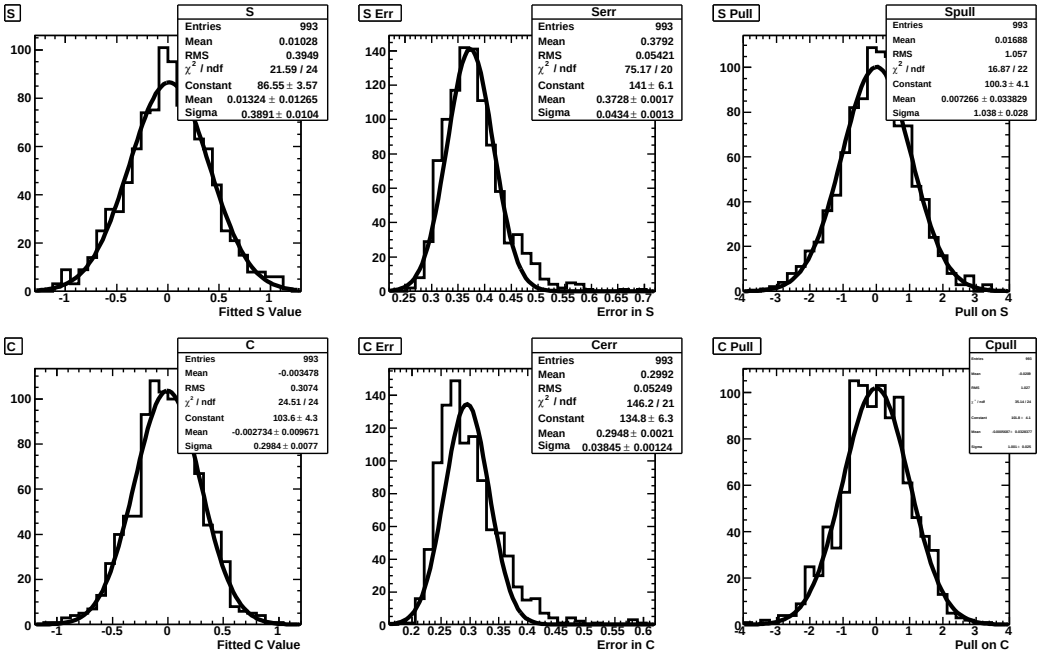

Figure 6.5: Results showing the S and C values and pulls as well as their errors obtained by performing 1,000 pure toy studies (rather than the signal-embedded toys discussed in Section 8.2). These are the results after the second stage in the maximum likelihood fit (also described in Section 8.2). These plots were produced using a cut on the BDT at 0.6 and result in the smallest error for the CP-violation parameter S. Thus, this value of the cut was used in the final running of the fit to data.

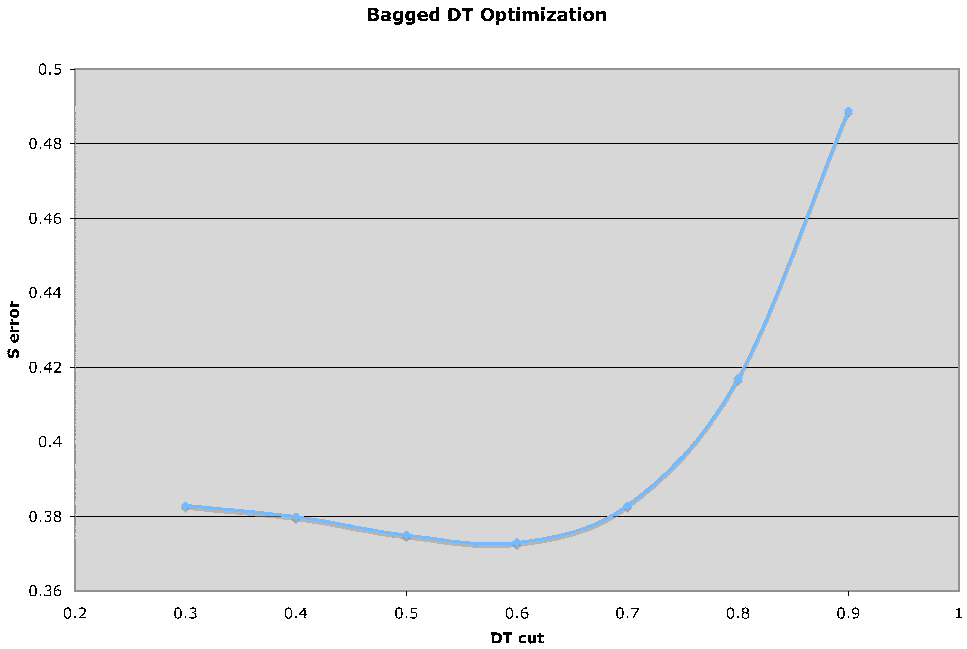

Figure 6.6: Error on the CP-asymmetry parameter S vs. BDT cut. The error on S is calculated by doing 1,000 pure toy studies for each BDT cut. The mean of the S error distribution is plotted above. The fitting strategy is discussed in Chapter 8.

Chapter 7

Expected Contributions and Fitting Categories

In this Chapter both the MC expectation for the contributions of the signal and various background components and the motivation for combining several of the background components into combined fitting categories are presented. The fit itself will be described in Chapter 8.

The expected contribution from each mode is equal to the estimated number of events for 468 fb^{-1} remaining in the fit region ($|\Delta E^*| < 0.3$, $m_{\rm ES} > 5.22$ and $|\Delta t| < 20$ps) after the selection criteria and BDT cut have been applied. To get this number we multiply the number of B pairs produced in the detector by the branching fraction of the appropriate decay mode, then divide by the total number of Monte Carlo generated events (for MC data sets see Section 4.3.1); this is the expected luminosity. An outline of how the signal and generic B luminosities

were calculated is illustrated in Tables 7.1 and 7.2. The continuum luminosities are listed in Table 4.1. Next, the selection criteria and BDT cuts are applied, after which the number of events remaining in the fit region are the amount expected.

Mode	$\mathcal{B}$ [15]	**nGen**	**Scale** $= \frac{(\mathcal{B})(nB)}{nGen}$
$B^0 \to \rho^0\gamma$	8.6e-7	650000	0.00062
$B^\pm \to \rho^\pm\gamma$	9.8e-7	650000	0.00070
$B^0 \to \omega\gamma$	4.4e-7	650000	0.00031
$B^0\bar{B}^0$	$\frac{1}{2}$	717995000	0.32
B^+B^-	$\frac{1}{2}$	708762000	0.33

Table 7.1: Scale Factor calculations for the $B \to (\rho/\omega)\gamma$ and generic B modes. The scale is the factor to be applied in order to produce a sample with the same luminosity as the data (468 fb^{-1}). The number of B events (nB) collected in the data is 465 million.

Mode	$\mathcal{B}$ [15]	$K^* \to K\pi$	$K_s \to \pi\pi$	**nGen**	**Scale** $= \frac{(\mathcal{B}s)(nB)}{nGen}$
$K^{*+} \to K^+\pi^0$	4.33e-5	$\frac{1}{3}$	n/a	2149000	0.0031
$K^{*0} \to K^+\pi^-$	4.21e-5	$\frac{2}{3}$	n/a	2149000	0.0061
$K^{*0} \to K^0_s\pi^0$	4.21e-5	$\frac{1}{3}\frac{1}{2}$	$\frac{2}{3}$	650000	0.0033
$K^{*+} \to K^0_s\pi^+$	4.33e-5	$\frac{2}{3}\frac{1}{2}$	$\frac{2}{3}$	2149000	0.0021

Table 7.2: Scale Factor calculations for the $B \to K^*\gamma$ modes. The scale is the factor to be applied in order to produce a sample with the same luminosity as the data (468 fb^{-1}). The number of B events (nB) collected in the data is 465 million.

7.1 Expected Yields

The expected contributions based on luminosity weighted MC which has been subjected to all skim, reduction, and BDT output cuts are summarized in Ta-

ble 7.3. The luminosity weighted MC projections of ΔE^*, $m_{\rm ES}$, and Δt are shown in Figures 7.1 through 7.12. A fit-region cut of $|\Delta E^*| < 0.3$, $m_{\rm ES} > 5.22$ and $|\Delta t| < 20$ps and a BDT cut at 0.6 have been applied to each of these MC data set projections. The expected yields are the respective integrals of each projection.

Mode	**Events**
$B^0 \to \rho^0\gamma$	75.05
$B^\pm \to \rho^\pm\gamma$	1.81
$B^0 \to \omega\gamma$	1.25
$K^{*0} \to K^+\pi^-$	31.89
$K^{*+} \to K^+\pi^0$	0.87
$K^{*+} \to K^0_s\pi^+$	21.60
$K^{*0} \to K^0_s\pi^0$	0.79
$B^0\bar{B}^0$	108.20
B^+B^-	114.00

Table 7.3: Number of expected signal and $B\overline{B}$ background fit-region events based on luminosity weighted MC (post-skim, reduction, and BDT cuts).

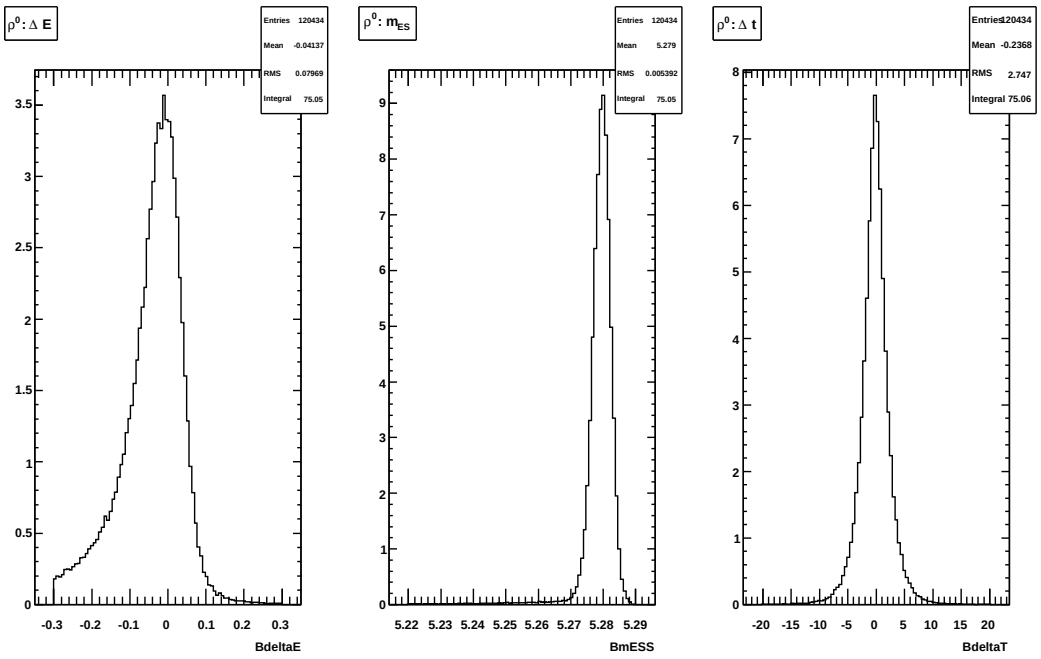

Figure 7.1: Luminosity weighted signal $B^0 \to \rho^0\gamma$ MC projections: ΔE^* (left), $m_{\rm ES}$ (center), and Δt (right). A fit-region cut of $|\Delta E^*| < 0.3$, $m_{\rm ES} > 5.22$ and $|\Delta t| < 20$ps and a cut on the BDT output at 0.6 have been applied to all projections. The expected yield is the integral of these luminosity weighted projections.

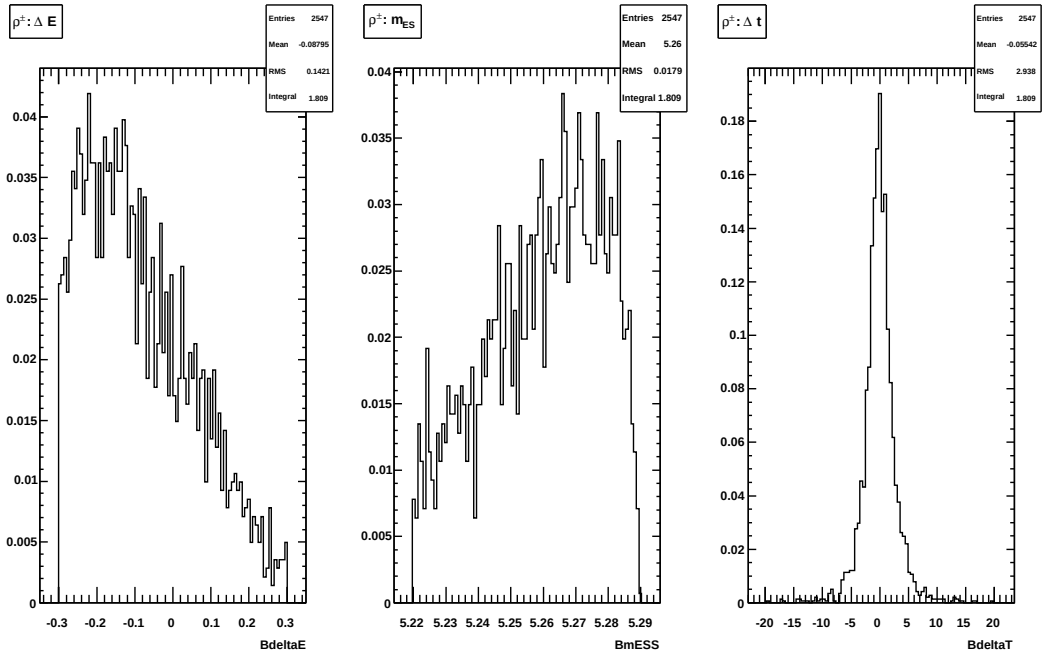

Figure 7.2: Luminosity weighted $\rho^{\pm}$ MC projections: ΔE^* (left), $m_{\rm ES}$ (center), and Δt (right). A fit-region cut of $|\Delta E^*| < 0.3$, $m_{\rm ES} > 5.22$ and $|\Delta t| < 20$ps and a cut on the BDT output at 0.6 have been applied to all projections. The expected yield is the integral of these luminosity weighted projections.

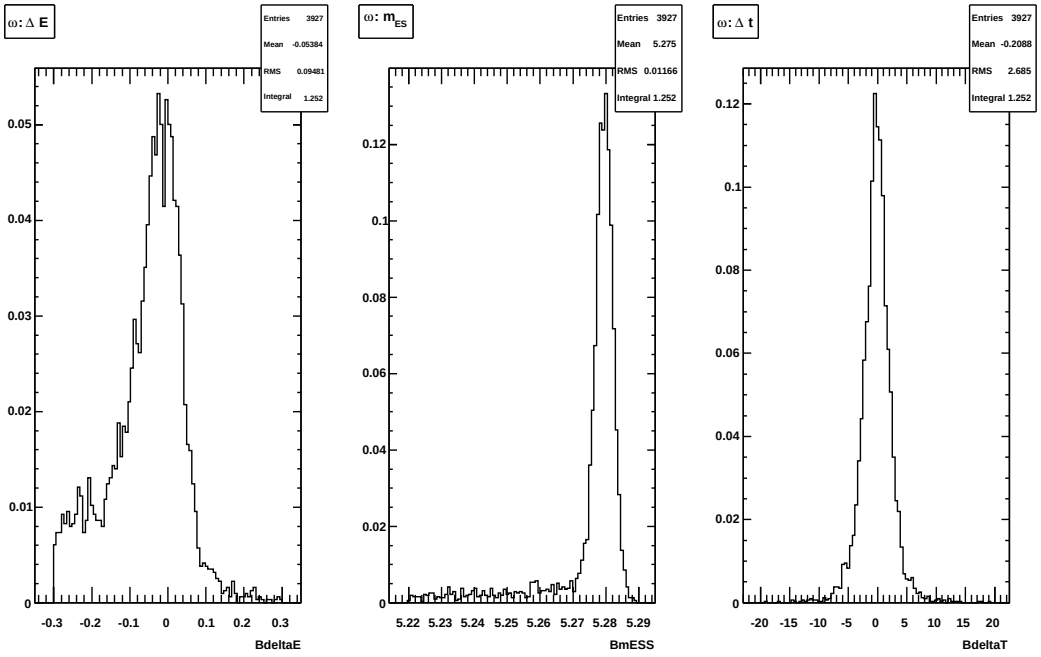

Figure 7.3: Luminosity weighted ω MC projections: ΔE^* (left), $m_{\rm ES}$ (center), and Δt (right). A fit-region cut of $|\Delta E^*| < 0.3$, $m_{\rm ES} > 5.22$ and $|\Delta t| < 20$ps and a cut on the BDT output at 0.6 have been applied to all projections. The expected yield is the integral of these luminosity weighted projections.

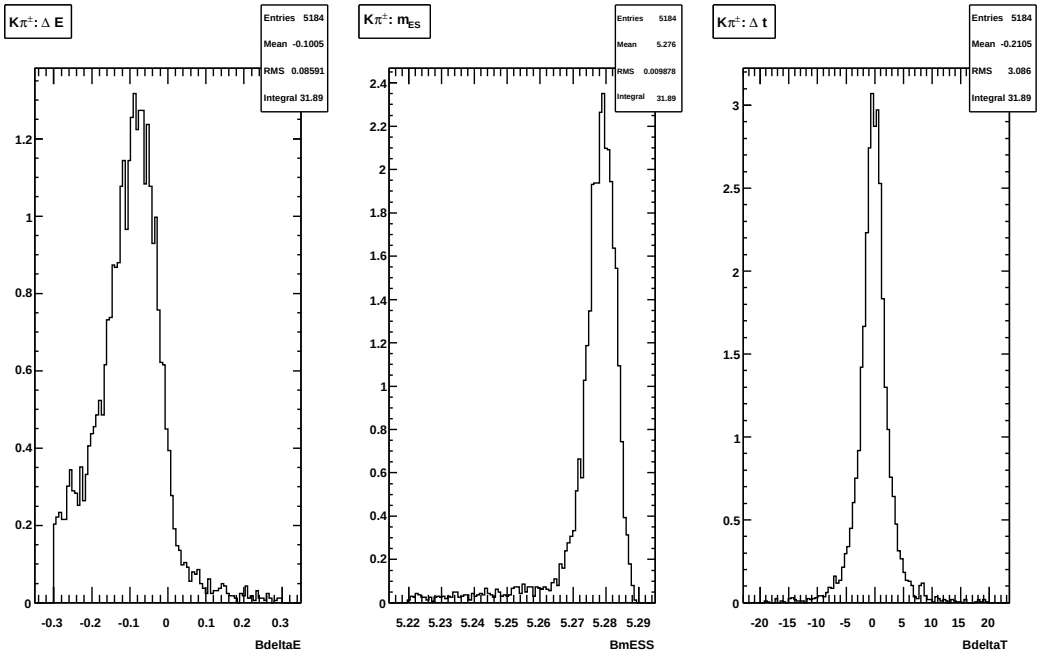

Figure 7.4: Luminosity weighted $K\pi^{\pm}$ MC projections: ΔE^* (left), $m_{\rm ES}$ (center), and Δt (right). A fit-region cut of $|\Delta E^*| < 0.3$, $m_{\rm ES} > 5.22$ and $|\Delta t| < 20$ps and a cut on the BDT output at 0.6 have been applied to all projections. The expected yield is the integral of these luminosity weighted projections.

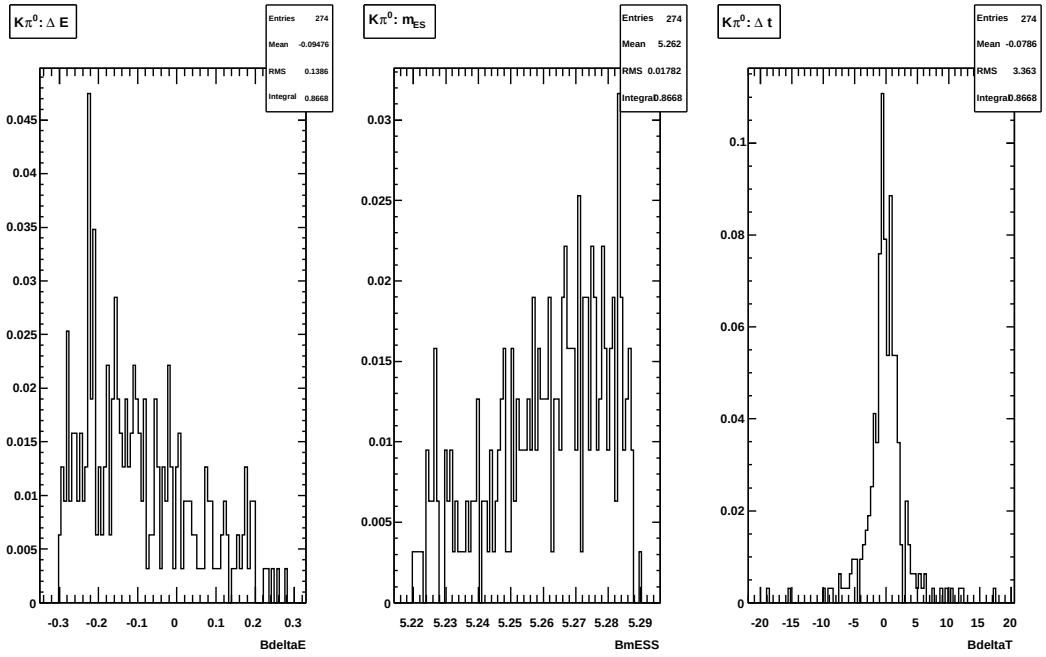

Figure 7.5: Luminosity weighted $K\pi^0$ MC projections: ΔE^* (left), $m_{\rm ES}$ (center), and Δt (right). A fit-region cut of $|\Delta E^*| < 0.3$, $m_{\rm ES} > 5.22$ and $|\Delta t| < 20$ps and a cut on the BDT output at 0.6 have been applied to all projections. The expected yield is the integral of these luminosity weighted projections.

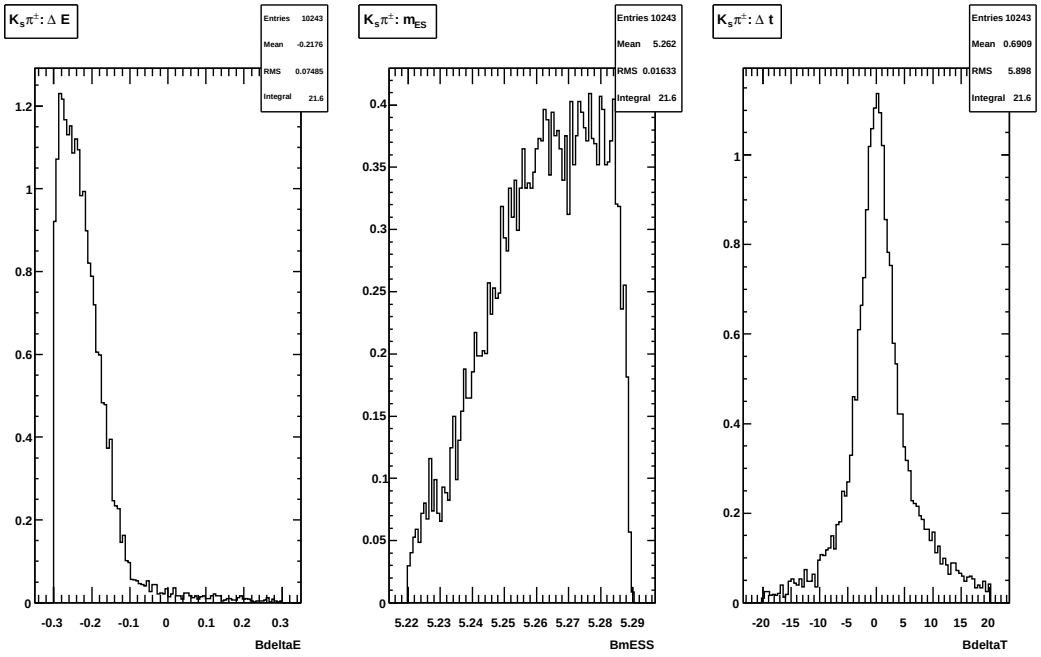

Figure 7.6: Luminosity weighted $K_s\pi^{\pm}$ MC projections: ΔE^* (left), $m_{\rm ES}$ (center), and Δt (right). A fit-region cut of $|\Delta E^*| < 0.3$, $m_{\rm ES} > 5.22$ and $|\Delta t| < 20$ps and a cut on the BDT output at 0.6 have been applied to all projections. The expected yield is the integral of these luminosity weighted projections.

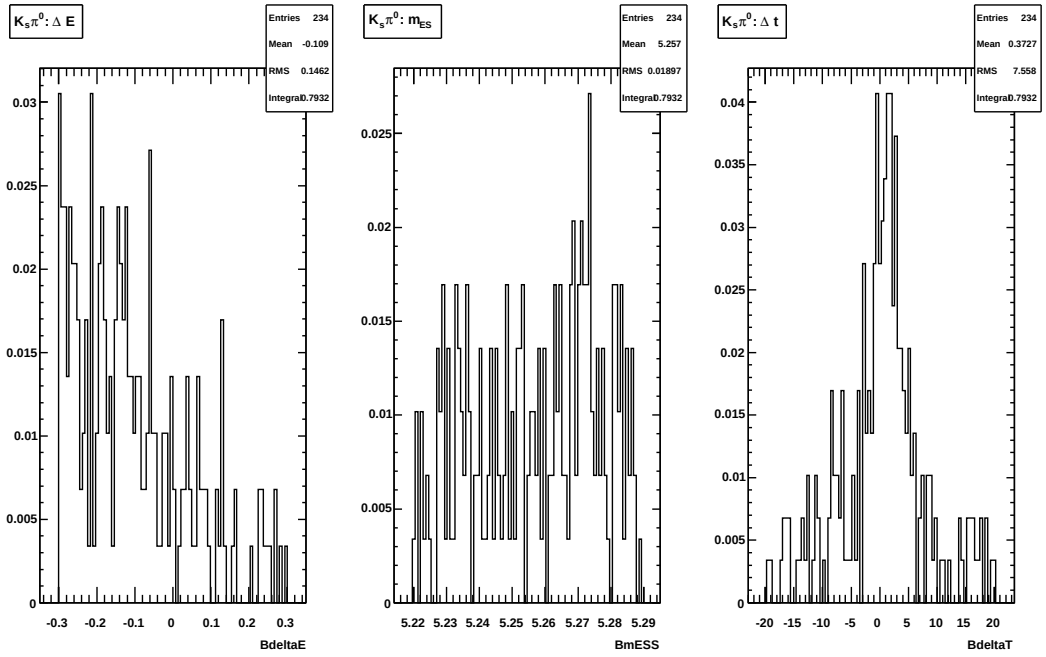

Figure 7.7: Luminosity weighted $K_s\pi^0$ MC projections: ΔE^* (left), $m_{\rm ES}$ (center), and Δt (right). A fit-region cut of $|\Delta E^*| < 0.3$, $m_{\rm ES} > 5.22$ and $|\Delta t| < 20$ps and a cut on the BDT output at 0.6 have been applied to all projections. The expected yield is the integral of these luminosity weighted projections.

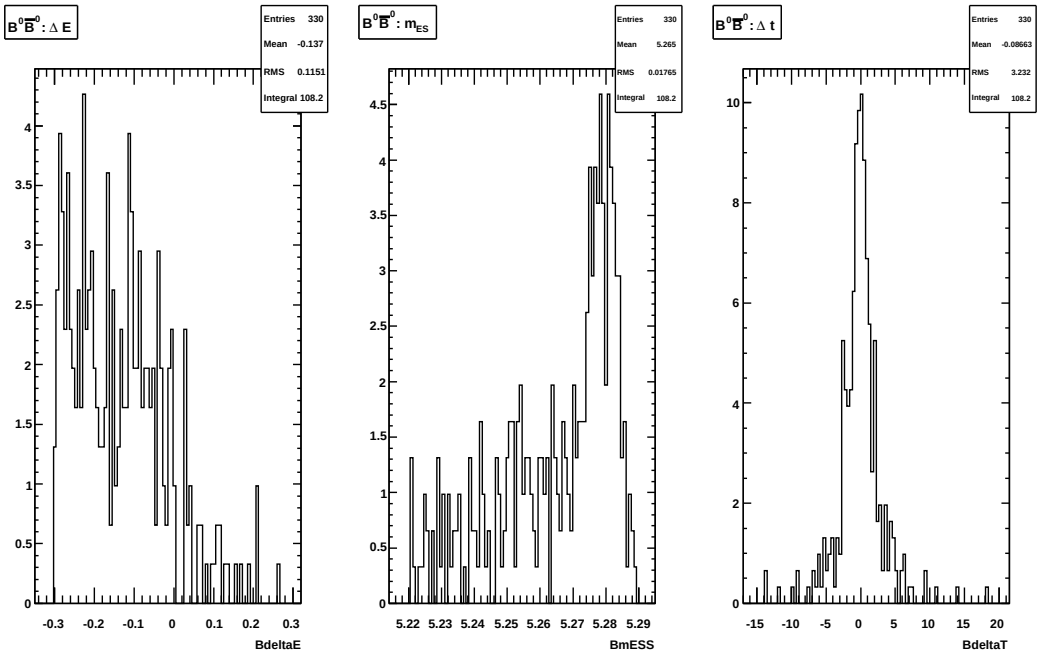

Figure 7.8: Luminosity weighted $B^0\bar{B}^0$ MC projections: ΔE^* (left), $m_{\rm ES}$ (center), and Δt (right). A fit-region cut of $|\Delta E^*| < 0.3$, $m_{\rm ES} > 5.22$ and $|\Delta t| < 20$ps and a cut on the BDT output at 0.6 have been applied to all projections. For the generic B modes an additional cut has been applied in order to avoid any $B \to X_d\gamma$ contributions which are accounted for in the signal cross-feed. The expected yield is the integral of these luminosity weighted projections.

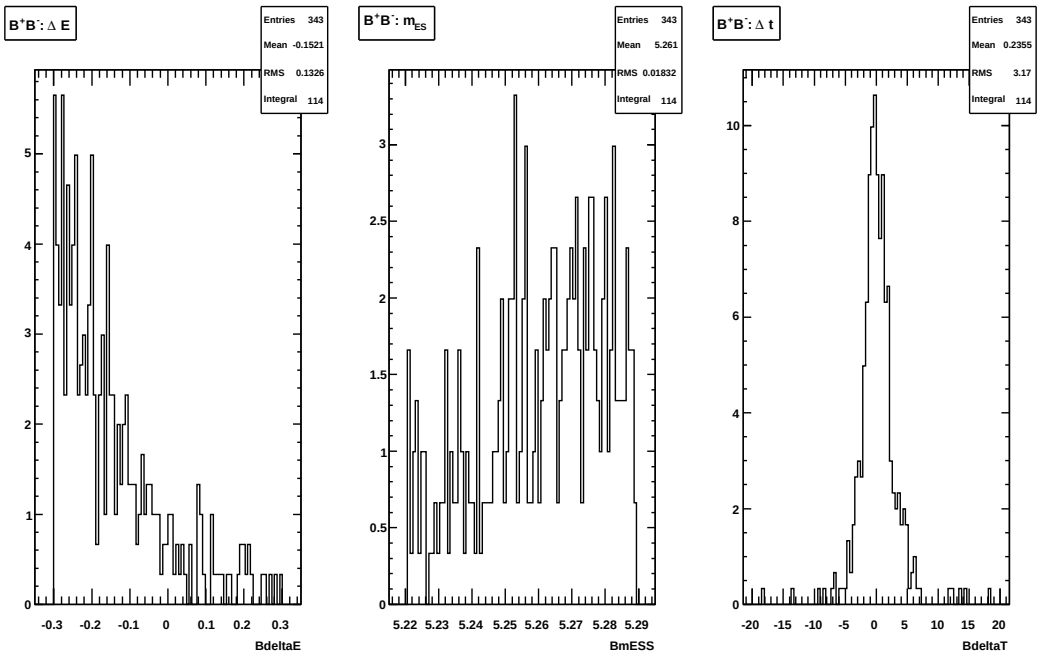

Figure 7.9: Luminosity weighted B^+B^- MC projections: ΔE^* (left), $m_{\rm ES}$ (center), and Δt (right). A fit-region cut of $|\Delta E^*| < 0.3$, $m_{\rm ES} > 5.22$ and $|\Delta t| < 20$ps and a cut on the BDT output at 0.6 have been applied to all projections. For the generic B modes an additional cut has been applied in order to avoid any $B \to X_d\gamma$ contributions which are accounted for in the signal cross-feed. The expected yield is the integral of these luminosity weighted projections.

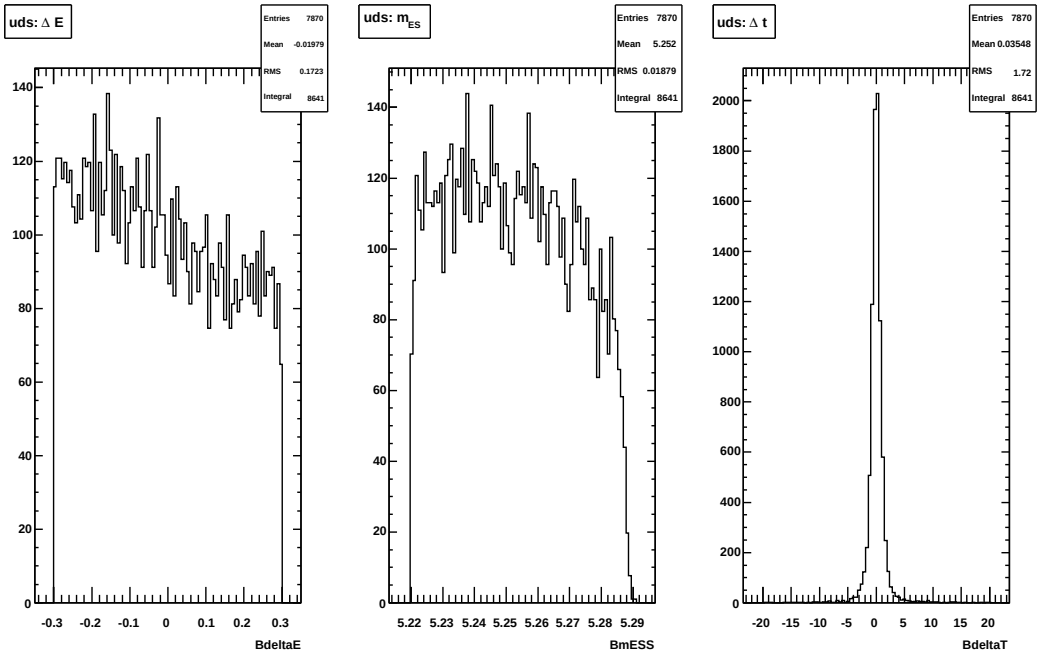

Figure 7.10: Luminosity weighted *uds* MC projections: ΔE^* (left), $m_{\rm ES}$ (center), and Δt (right). A fit-region cut of $|\Delta E^*| < 0.3$, $m_{\rm ES} > 5.22$ and $|\Delta t| < 20$ps and a cut on the BDT output at 0.6 have been applied to all projections. The expected yield is the integral of these luminosity weighted projections.

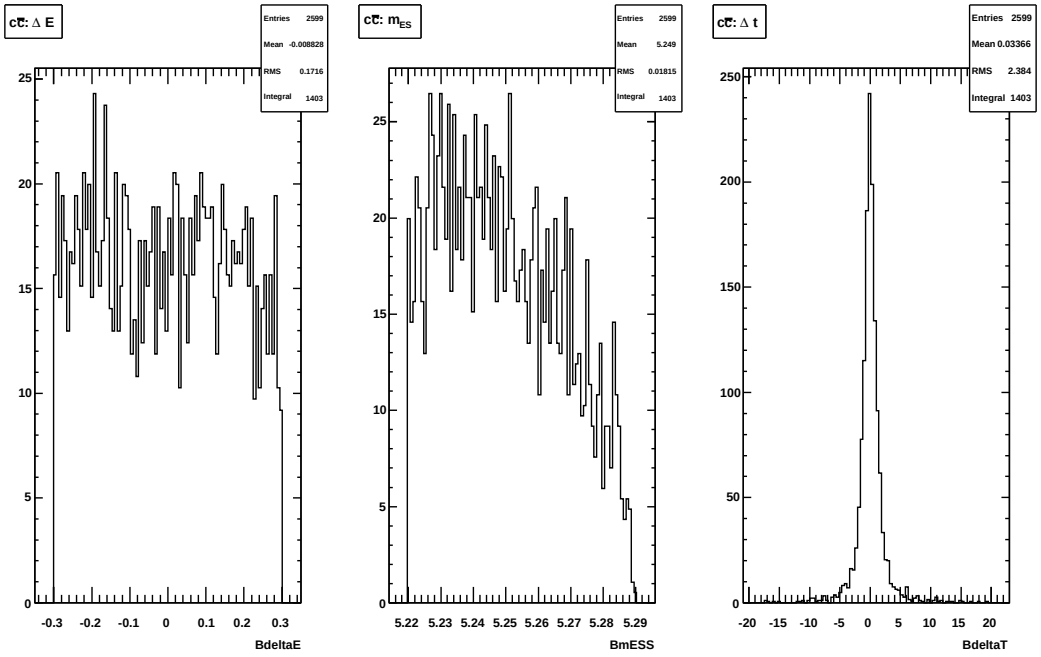

Figure 7.11: Luminosity weighted $c\bar{c}$ MC projections: ΔE^* (left), $m_{\rm ES}$ (center), and Δt (right). A fit-region cut of $|\Delta E^*| < 0.3$, $m_{\rm ES} > 5.22$ and $|\Delta t| < 20$ps and a cut on the BDT output at 0.6 have been applied to all projections. The expected yield is the integral of these luminosity weighted projections.

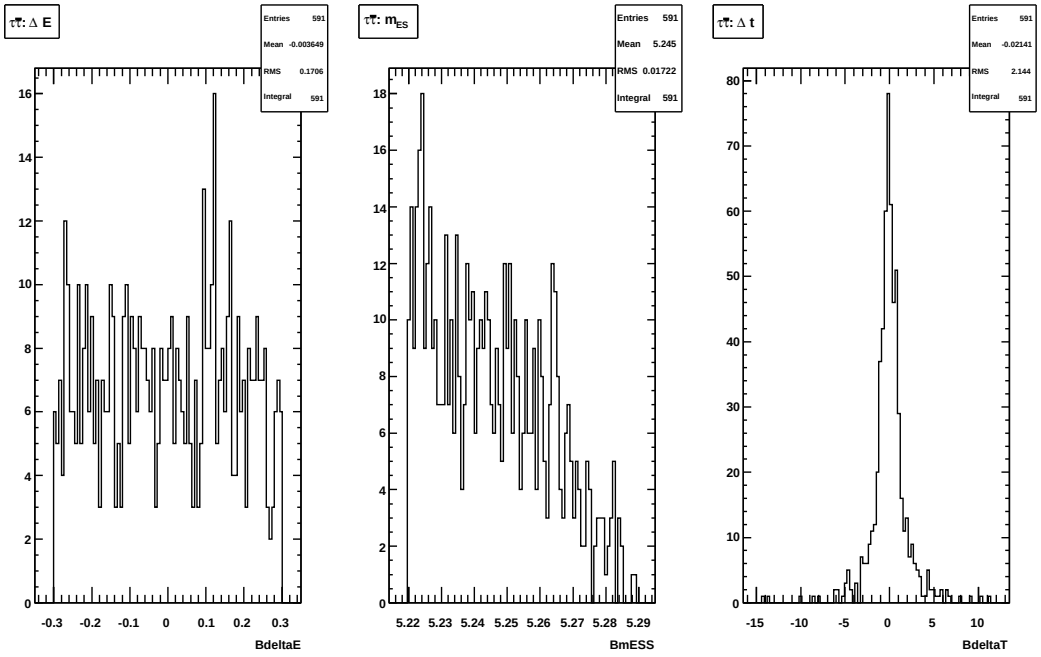

Figure 7.12: Luminosity weighted $\tau\bar{\tau}$ MC projections: ΔE^* (left), $m_{\rm ES}$ (center), and Δt (right). A fit-region cut of $|\Delta E^*| < 0.3$, $m_{\rm ES} > 5.22$ and $|\Delta t| < 20$ps and a cut on the BDT output at 0.6 have been applied to all projections. The expected yield is the integral of these luminosity weighted projections.

7.2 Fitting Categories

Various backgrounds are more easily identified when grouped together; one probability density function (PDF) shape can describe a group of backgrounds having similar distributions in the fitting variables while providing a more simple fitting algorithm. In Chapter 4 the continuum and various $B\overline{B}$ backgrounds were outlined, and the various $B\overline{B}$ background modes described there are combined into three separate categories based on the ΔE^* and $m_{\rm ES}$ fit-region distributions. Referring again to Figures 7.1 through 7.12 the ρ^+, ω, $K^{*0} \to K^+\pi^-$, and $K^{*+} \to K^+\pi^0$ modes all peak considerably in $m_{\rm ES}$ and have an offset peak in ΔE^*. This group of decay modes is given one PDF shape and is referred to as peaking cocktail 1. The modes $K^{*+} \to K^0_s\pi^+$ and $K^{*0} \to K^0_s\pi^0$ similarly have an offset peak in ΔE^* but do not peak in $m_{\rm ES}$; this group is referred to as peaking cocktail 2. The rest of the $B\overline{B}$ modes are lumped together in the generic category. The generic B backgrounds peak less in the kinematic variables than the peaking cocktails. The PDF shapes for each fitting category (described in the next section), generic B, continuum, peaking cocktail 1, and peaking cocktail 2, are shown in Figure 8.2.

Chapter 8

Fitter

The fits for each mode employ an extended unbinned maximum likelihood technique using `RooFit` [30] - a general maximum likelihood fitter based on the `ROOT` data analysis framework. Built from signal and background components, the probability density functions (PDFs) for all events are combined and augmented by a Poisson variation factor for the signal yield; thus the yield and CP-violating asymmetry parameters S and C, being free parameters in the fit, can be extracted directly from the results.

8.1 Maximum Likelihood Fit

The likelihood function $\mathcal{L}$ over a set of independent variables $\vec{x}$ is constructed from a set of PDFs $P(\vec{x})$ for M candidate signal and background hypotheses (ours being the ρ^0 signal, continuum, generic $B\overline{B}$, peaking cocktails 1, and 2 outlined

	$m_{\rm ES}$	ΔE^*	Δt
Signal	HistPDF	HistPDF	BCPGenDecay
Continuum	Argus	Polynomial	Res. Function
$B\overline{B}$	HistPDF	HistPDF	HistPDF
Peaking 1	HistPDF	HistPDF	HistPDF
Peaking 2	HistPDF	HistPDF	HistPDF

Table 8.1: `RooFit` PDF shapes used in the yield fit (described in subsequent subsections).

in Section 7.2) and for N events is defined as

$$\mathcal{L} = \exp\Big(-\sum_{i=1}^{M} n_i\Big) \cdot \Big(\prod_{j=1}^{N}\Big[\sum_{i=1}^{M} n_i P_i(\vec{x}_j)\Big]\Big) \tag{8.1}$$

where n_i is the yield (the number of events) for each candidate hypothesis i. For this analysis, $\mathcal{L}$ is constructed as if the variables $\vec{x}$ are uncorrelated for each candidate hypothesis. In the fit, $\mathcal{L}$ is maximized over the parameter space to give the most likely values of the floating parameters. The number of signal events and the CP-violating asymmetry parameters S and C are thus maintained as floating parameters of the fit.

We perform a 3D likelihood fit in this analysis with the $m_{\rm ES}$, ΔE^*, and Δt distributions as the inputs $\vec{x}_j$. The signal and background PDF components are summarized in Table 8.1 and are described in more detail in the following subsections. We do the fit in two stages. The first stage considers only $m_{\rm ES}$ and ΔE^* and extracts the value of the signal yield. In the second stage $m_{\rm ES}$ is restricted to values within the signal region, and Δt is included as a third independent variable, allowing for the extraction of S and C.

8.2 Fitting Method

The strength of each $m_{\rm ES}$, ΔE^*, and Δt shape, its contribution to the total PDF, are determined by signal MC and are fixed in the final fit. The $B\overline{B}$ and peaking background shapes are determined using generic MC samples while the mis-tag rates, reconstruction efficiency flavor differences, and resolution function parameters for the time-dependent part of the fit are given by the *BABAR* B-tagging group. The S and C values are floated in and then extracted from the final fit. Systematic errors due to resolution function parameters are discussed in Section 9.

The fit employed consists of two stages. In the first stage the Δt shape is not included in the overall PDF, thus we initially use a 2D $m_{\rm ES}$ and ΔE^* model. This model is split by tagging category where the fraction of the overall yields for signal and all backgrounds are different in each tagging category. For everything except continuum the fraction of the overall yield in each category is fixed according to numbers provided by the B-tagging group which are listed in Table 5.3. For continuum these fractions are allowed to float. For signal, the overall yield floats, and the fractions remain fixed. All other background yields are fixed. The floating parameters in the first stage fit are: signal yield, continuum background yield (split by tagging category), $m_{\rm ES}$ Argus parameter (see Section 8.4) and ΔE^* polynomial coefficient (see Section 8.4.2) .

In the second stage the Δt component is included and all the parameters which floated in stage 1 are fixed to the values yielded by that fit. The Δt shape is dependent on the tagging category. In this fit only the S and C parameters are

allowed to float.

This configuration was decided upon as it appeared in tests to give the most stable performance in the second stage. Without the division of the fit into these two steps it was found to be prone to failure. With the division of the fit into these steps the uncertainties on the signal yield are not accounted correctly; this inconsistency is currently under investigation and is what makes the results of this thesis preliminary.

8.3 Signal PDF

The following sections describe the various PDF components for the signal shape.

8.3.1 $m_{\rm ES}$ and ΔE^*

For these types of *BABAR* analyses the fitting range, defined by cuts on the kinematic variables ΔE^* and $m_{\rm ES}$, is traditionally established as 5.22 to 5.3 GeV in $m_{\rm ES}$ and -0.3 to 0.3 GeV in ΔE^* [4]. This full range of $m_{\rm ES}$ was used in the first stage of the fit. A tighter cut on $m_{\rm ES}$ was used in the second stage of the fit. This tighter cut isolates the signal region of 5.26 to 5.29 GeV (see Section 3.1).

A 2D histogram PDF built from MC is used to describe the signal ΔE^* and $m_{\rm ES}$ shapes in the fitting range. The `RooFit RooHistPdf` takes an input histogram and represents its shape as a PDF. The histogram contents are explicitly

scaled to obtain proper normalization.

8.3.2 Δt

The signal Δt, in the fit region of $|\Delta t| < 20$ ps, is parametrized using the probability for interference between mixing and decay defined in Section 3.1.3 and reproduced here:

$$\mathcal{P}_{\pm}(\Delta t|S,C) = \frac{1}{4\tau_B} e^{-|\Delta t|/\tau_B} \left[1 \pm S\sin(\Delta m \Delta t) \mp C\cos(\Delta m \Delta t)\right], \tag{8.2}$$

where the upper signs correspond to tagged B^0's and the lower signs correspond to tagged $\overline{B}^0$'s. This is the probability distribution for a final state with one CP eigenstate and one self-tagging (identifies the B flavor at the time of decay) state. Here τ_B is the B^0 lifetime, Δm is the mass difference between the two B^0 mass eigenstates and Δt is the time difference ($t_{\rm rec} - t_{\rm tag}$). The parameter S is a measure of CP-violation due to interference between B^0 decays with and without mixing while the parameter C is the direct CP-asymmetry.

This probability distribution is considered for each of the six different tagging categories (see [33] for a description of `Tag08`). The untagged events constrain the branching fraction but not S or C. We must account for the average mis-tag probability w, the difference Δw in that probability between B^0 and $\overline{B}^0$ tags, and the tagging efficiency difference μ. Equation 8.2, adjusted by these factors, is the

`RooFit BCPGenDecay` PDF

$$\mathcal{P}_{\pm}(\Delta t|S,C) = \frac{1}{4\tau_B} e^{-|\Delta t|/\tau_B}\{1 \mp \Delta w \pm \mu(1-2w) \pm [(1-2w) \pm \mu(1 \mp \Delta w)] \\ [S\sin(\Delta m \Delta t) - C\cos(\Delta m \Delta t)]\}. \tag{8.3}$$

As before, the upper signs correspond to tagged B^0 mesons and the lower signs correspond to tagged $\bar{B}^0$ mesons.

To account for the *BABAR* detector's limited vertex resolution Equation 8.3 is convolved with a resolution function on Δt. This signal resolution function is the sum of three gaussians (core, tail, and outlier). The σ and mean of the core and tail gaussians scale with $\sigma_{\Delta t}$, which is set on an event-by-event basis.

As with previous *BABAR* analyses (see [31]) due to the large correlation between the resolution function parameters, the tail gaussian σ is fixed to be 3.0ps, the value of which was derived from Monte Carlo studies. The effect of fixing the tail σ must be considered in the systematic error determination (see Section 9). The fixed values used for the triple gaussian parameters are:

- Core σ: Split between lepton-tagged events (1.1033 ps) and non-lepton-tagged events (1.0106 ps)
- Core Bias: Split between lepton-tagged events (-0.0504 ps) and non-lepton-tagged events (-0.2408 ps)
- Core fraction: 0.8758

- Tail σ: 3.0 ps (Not split between tagging categories)
- Tail Bias: -1.03 ps (Not split between tagging categories)
- Outlier σ: 8.0 ps (Not split between tagging categories)
- Outlier Bias: 0.0 ps (Not split between tagging categories)
- Outlier fraction: 0.0033

Only the S and C parameters float in the final fit to data.

The average mis-tag probabilities w and Δw depend on the tagging category. A single value of the resolution function's core mean and width are used for all but the lepton-tag category, as is done in [32]. All of the tagging parameters are fixed to the B-tagging group's results of the B_{flav} fit listed in Table 5.3.

Figure 8.1 shows each of the signal histograms m_{ES}, ΔE^*, and BCPGenDecay Δt PDFs.

8.4 Continuum PDF

8.4.1 m_{ES}

We use an ARGUS function with an endpoint set on an event-by-event basis by the measured beam energy: $m_0 = \sqrt{s}/2$. The conditional PDF is

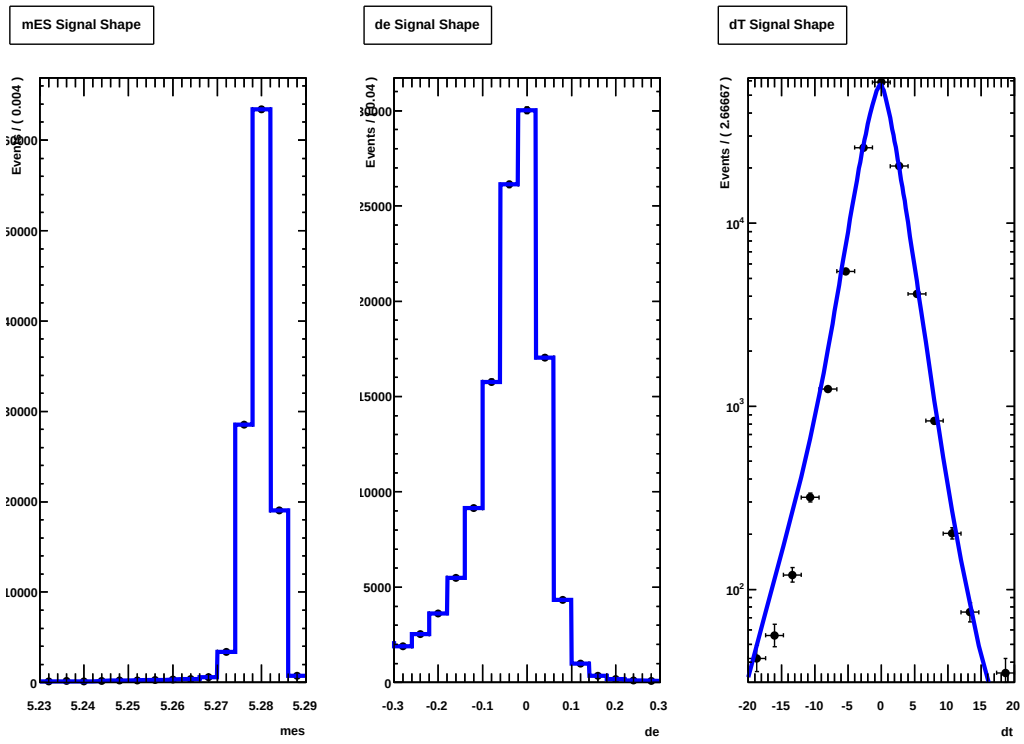

Figure 8.1: The signal ΔE^*, $m_{\rm ES}$, and Δt PDF shapes. The ΔE^* and $m_{\rm ES}$ PDFs are MC generated histograms while the Δt PDF is the decay probability function convolved with a triple gaussian resolution function, each described in Section 8.3.

$$\mathrm{ARGUS}(m_{\mathrm{ES}}|m_0, c) = m_{\mathrm{ES}}[1 - (m_{\mathrm{ES}}/m_0)^2]^{\frac{1}{2}} \times \exp\{c[1 - (m_{\mathrm{ES}}/m_0)^2]\}, \quad (8.4)$$

where c is the shape parameter. Because the distribution of the average endpoint m_0 is the same for signal and background events, there can be no bias due to not including a PDF for it. The c parameter is allowed to float in the first stage fit over the full range of m_{ES}, and is fixed to its best fit value of -25.3 for the second stage fit over the restricted range in m_{ES}.

8.4.2 ΔE^*

For continuum ΔE^* we use a second order polynomial

$$f(\Delta E^*|P01, P02) = 1 + P01 \cdot \Delta E^* + P02 \cdot \Delta E^{*2}. \quad (8.5)$$

The $P01$ and $P02$ parameters are allowed to float in the first stage fit, and are fixed to their best fit values for the second stage fit.

8.4.3 Δt

A delta function smeared with a triple Gaussian is used for the continuum Δt shape. The values used for the triple gaussian parameters fixed after the first stage fit are:

- Core σ: 1.1 ps (floated in first stage fit, then fixed to this value)
- Core Bias: 0.02 ps (floated in first stage fit, then fixed to this value)
- Core fraction: 0.92 (floated in first stage fit, then fixed to this value)
- Tail σ: 3.0 ps (fixed in first and second stage fits)
- Tail Bias: 0.02 ps (floated in first stage fit, then fixed to this value)
- Outlier σ: 8.0 ps (fixed in first and second stage fits)
- Outlier Bias: 0.0 ps (fixed in first and second stage fits)
- Outlier fraction: 0.04 (fixed in first and second stage fits)

8.5 $B\overline{B}$ PDF

A histogram PDF built from the product of three one-dimensional histograms derived from MC distributions is used to describe the $B\overline{B}$ background. The ΔE^*, $m_{\rm ES}$, and Δt shapes are used to build the PDF.

8.6 Peaking Cocktail 1 PDF

The first peaking cocktail, described in Section 7.2, is a combination of ρ^+, ω, $K^{*0} \to K^+\pi^-$, and $K^{*+} \to K^+\pi^0$, the largest contributor being the K^+ mode. A

histogram PDF built from the product of three one dimensional histograms derived from MC distributions is used to describe the peaking cocktail 1 background ΔE^*, $m_{\rm ES}$, and Δt shapes.

8.7 Peaking Cocktail 2 PDF

The second peaking cocktail is a combination of the $K^{*+} \to K^0_s\pi^+$ and $K^{*0} \to K^0_s\pi^0$ modes also described in Section 7.2. A histogram PDF built from the product of three one dimensional histograms derived from MC distributions is used to describe the peaking cocktail 2 background ΔE^*, $m_{\rm ES}$, and Δt shapes.

Figure 8.2 shows the background PDF components including the combined charged and neutral $B\overline{B}$ histograms, the continuum Argus, polynomial, and resolution function, and the first and second peaking background histograms.

8.8 Signal Embedded MC Toy Studies

In order to validate the fitting procedure a large sample of "toy Monte Carlos" were generated. For each toy Monte Carlo, signal and background distributions were generated according to the PDFs described in the preceding sub-sections assuming $S = C = 0$. A Poisson fluctuated number of signal events with a mean corresponding to the expected yield was selected from the signal MC and added in. The fit, as described above, was then applied to each such toy Monte Carlo.

The expected number of signal events, its error and the pull from the expected

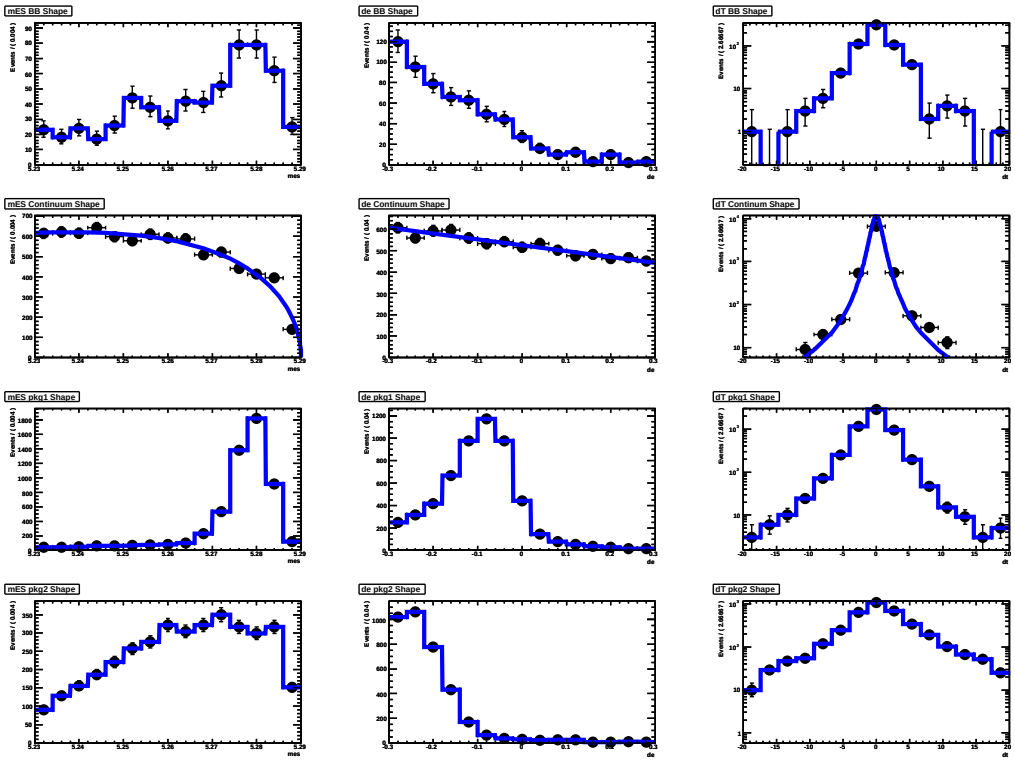

Figure 8.2: The various background PDF shapes. Left to right are $m_{\rm ES}$, ΔE^*, and Δt. The top row is the combined charged and neutral $B\overline{B}$ background 2D histogram, then continuum, the first peaking background 2D histogram (ρ^+, ω, $K^{*0} \to K^+\pi^-$, $K^{*+} \to K^+\pi^0$), and the second peaking background 2D histogram ($K^{*+} \to K^0_s\pi^+$ and $K^{*0} \to K^0_s\pi^0$).

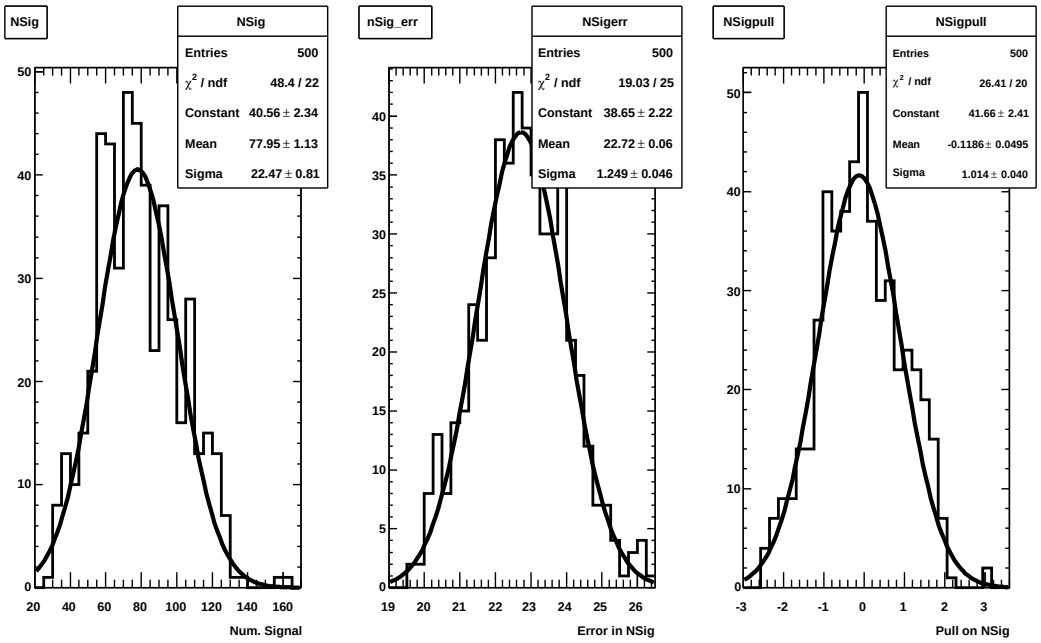

Figure 8.3: Signal yields, errors, and pulls after 500 signal embedded toy studies after the first stage fit.

value after the first stage of the fit is shown in Figure 8.3 for a sample of 500 toy Monte Carlo trials. The mean of 78.0 is within 6 events of the expected value. The S and C parameters and their pulls and errors after the second stage of the fit are shown in Figure 8.4. Both of these stages employed a cut of 0.6 on the BDT output. The mean values of S and C are both within 1% of their expected value of 0. The mean errors on S and C are 0.39 and 0.31 respectively, indicating that the fit is achieving good precision for the CP-violating parameters of interest.

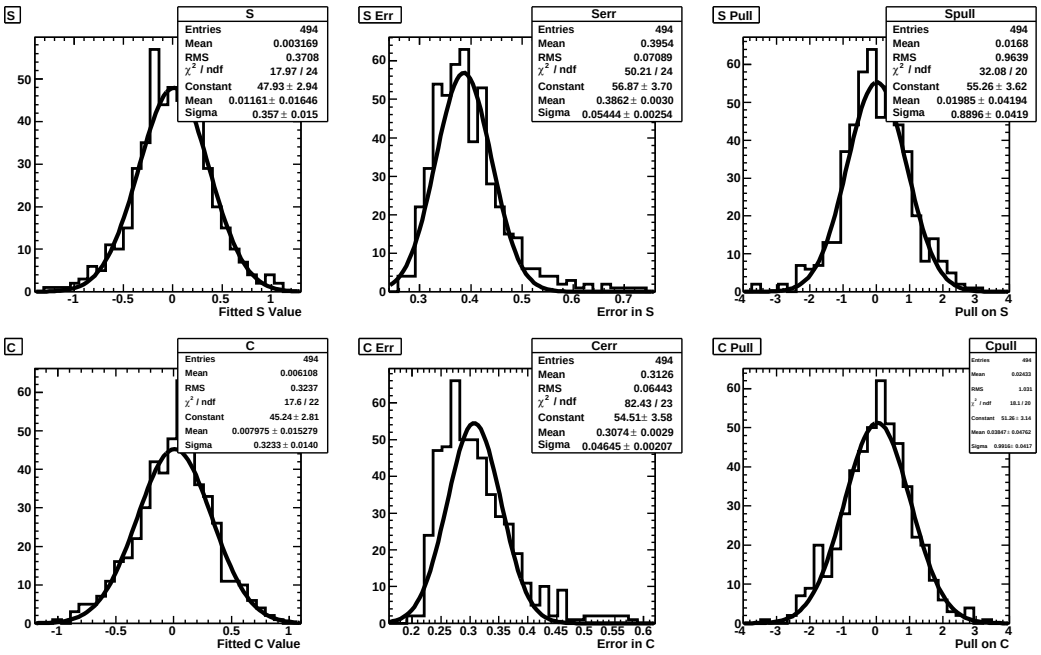

Figure 8.4: S and C values, errors, and pulls after 500 signal embedded toy studies after the second stage fit.

8.9 Fit to Data

In the first 2D $m_{\rm ES}$ and ΔE^* fit, the floated signal yield, continuum background (split by tagging category), $m_{\rm ES}$ Argus parameter, and ΔE^* polynomial coefficient are found and listed in Table 8.2. Figure 8.5 shows the result of the first stage fit, in comparison with data, in term of projections onto the $m_{\rm ES}$, ΔE^*, and Δt axes of the fitting space. The signal yield, nsig2D, is 26 ± 16 events, much lower than the expected number of 73 ± 9 events. For a much tighter cut of 0.9 on the BDT output a yield of 23 ± 9 events is observed, considerably closer to its expected yield of 38 ± 6. A set of fits performed as a function of the BDT cut are shown in Chapter 9.1 as part of a systematic uncertainty investigation. While this behavior is not yet understood we continue to use the BDT cut of 0.6, which was suggested by the optimization during the blind phase of the analysis. An exploration of the selection and fitting efficiencies making use of the copious K^* control sample is underway and is expected to shed light on this problem.

These parameters are fixed and the second stage $m_{\rm ES}$, ΔE^*, and Δt combined fit is run to derive the values of S and C. The resulting fit when applied to the full *BABAR* data-set is shown in Figure 8.5. The CP-violation parameters extracted from the fit are:

$$C = 0.79 \pm 0.51(\text{stat}) \tag{8.6}$$

$$S = 0.38 \pm 0.54(\text{stat}) \tag{8.7}$$

No significant difference from zero is observed given the large uncertainties of the extracted values. The errors are substantially larger than the range of ± 0.3

Name	Value	Error
argpar	-13.0055	2.1694
deP01	-0.144874	0.021703
nbkg2D_08T0	2777.62	53.40
nbkg2D_08T1	34.7275	6.9895
nbkg2D_08T2	181.893	14.368
nbkg2D_08T3	602.101	25.353
nbkg2D_08T4	720.810	27.536
nbkg2D_08T5	1317.90	37.02
nbkg2D_08T6	936.400	31.061
nsig2D	25.9193	16.0983

Table 8.2: Values found in the first stage fit for the floating parameters in the 2D $m_{\rm ES}$ and ΔE^* fit. These parameters are fixed and the second stage $m_{\rm ES}$, ΔE^*, and Δt combined fit is run to derive the values of S and C

to ± 0.35 expected from the MC toy studies. Presumably this is due to the low observed yield which greatly reduces the statistics available to the determination of the CP-violating parameters.

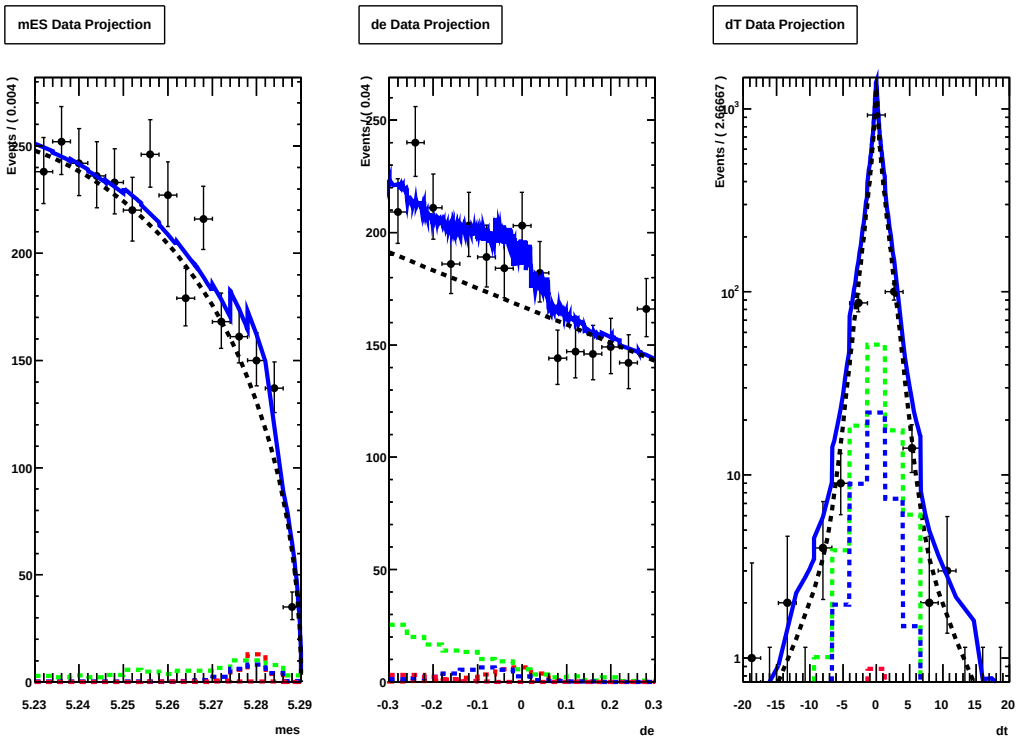

Figure 8.5: Projections of the results from the first stage data fit to, from left to right, $m_{\rm ES}$, ΔE^*, and Δt. In each projection the red curve is the $B^0 \to \rho^0\gamma$ signal, the black curve is the continuum background, the green curve is the generic $B\overline{B}$ background, the blue curve is the first peaking cocktail, and the pink curve is the second peaking cocktail.

Chapter 9

Systematics

Although this thesis will not present a final result that is appropriate for publication we have performed several systematic studies which establish the scale of systematic error on the results for the CP-violation parameters S and C.

9.1 BDT Output Cut

The small yield of $B^0 \to \rho^0\gamma$ events for the chosen BDT cut of 0.6 raises a concern that the effect of the BDT cut on the signal may not be well understood. To explore this we varied the cut between 0.3 and 0.9 re-doing both stages of the fit for each value of the cut. Figures 9.1 through 9.7 show the first stage fit results over the range of BDT cuts from 0.3 to 0.9. The yield is seen to vary across the small range between 34 and 22 while the continuum background is significantly suppressed at higher values of the BDT cut. The fit-values of S and C vary

between 0.05 and 0.63 (for S) and between -0.3 and 1.08 (for C), respectively. For S the errors seem to vary statistically with no clear trend observed as the BDT cut is increased, while for C it seems that there may be a decrease of the fit-value as the BDT cut increases and the sample becomes more pure. Although this may indicate that the poorly understood effect of the BDT cut may be compromising the ability to measure C, the measurement of S, which is the primary result of this thesis, seems not to be overly sensitive to the value of the BDT cut. We assign a preliminary systematic error of ± 0.15 which yields a $\pm 1\sigma$ band which covers half the range of the difference between the minimum and maximum fit-value of S. The corresponding error on C, estimated in the same way, is ± 0.35.

9.2 Fix Δt Resolution Function Parameters

Using the limited statistics of the $B^0 \to \rho^0\gamma$ signal to fit simultaneously for the Δt resolution parameters may subject the fit to instabilities. To explore this a number of parameters were constrained in an alternative strategy to performing the second stage of the fit. The triple gaussian core and outlier fractions in the signal and continuum background Δt resolution function were fixed to 100% and 0% respectively while the continuum function's core and tail bias were also fixed to their nominal values. This alternative fit was performed (see Figure 9.8) using the nominal BDT cut of 0.6 resulting in a change in S of 0.30 and in C of 0.02. We must therefore estimate an uncertainty of 0.30 on the S parameter and of negligible size for C due to the modeling of the Δt resolution function.

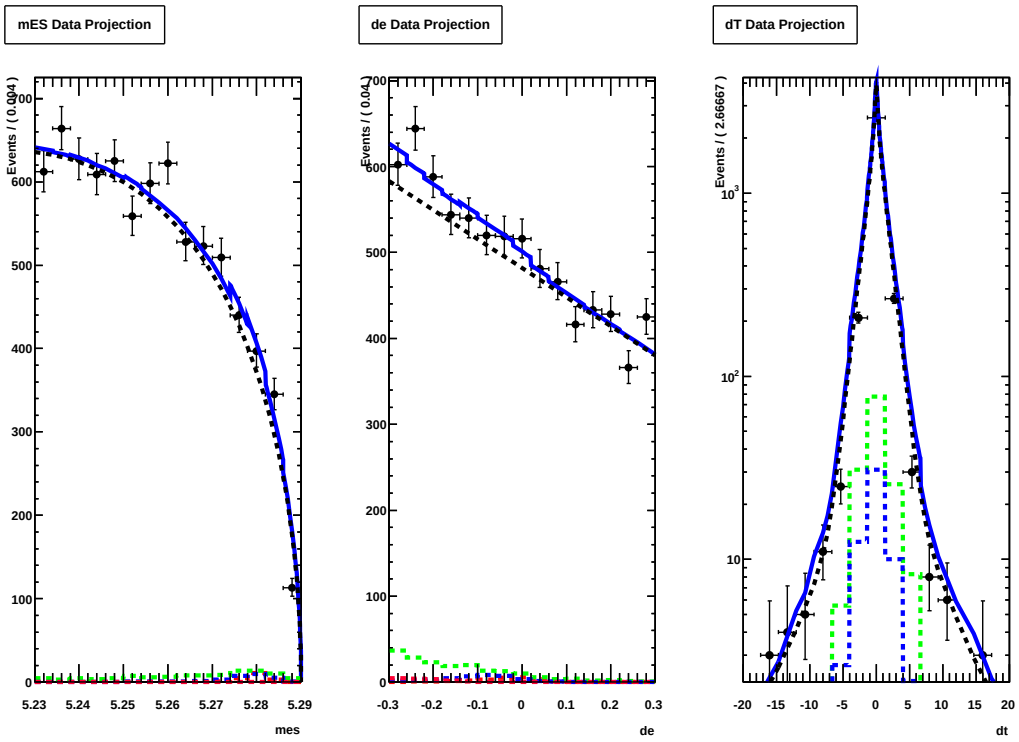

Figure 9.1: Shown above are, from left to right, $m_{\rm ES}$, ΔE^*, and Δt projections of the first stage fit with the data employing a BDT output > 0.3 cut. In each projection the red curve is the $B^0 \to \rho^0\gamma$ signal, the black curve is the continuum background, the green curve is the generic $B\overline{B}$ background, the blue curve is the first peaking cocktail, and the pink curve is the second peaking cocktail.

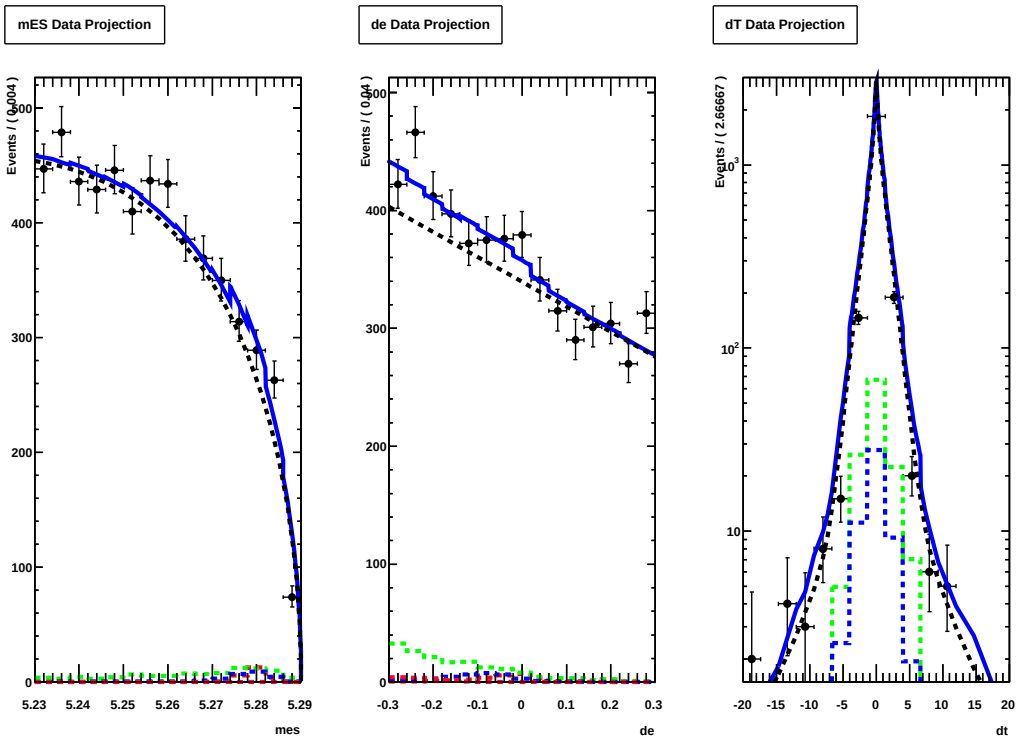

Figure 9.2: Shown above are, from left to right, $m_{\rm ES}$, ΔE^*, and Δt projections of the first stage fit with the data employing a BDT output > 0.4 cut. In each projection the red curve is the $B^0 \to \rho^0\gamma$ signal, the black curve is the continuum background, the green curve is the generic $B\overline{B}$ background, the blue curve is the first peaking cocktail, and the pink curve is the second peaking cocktail.

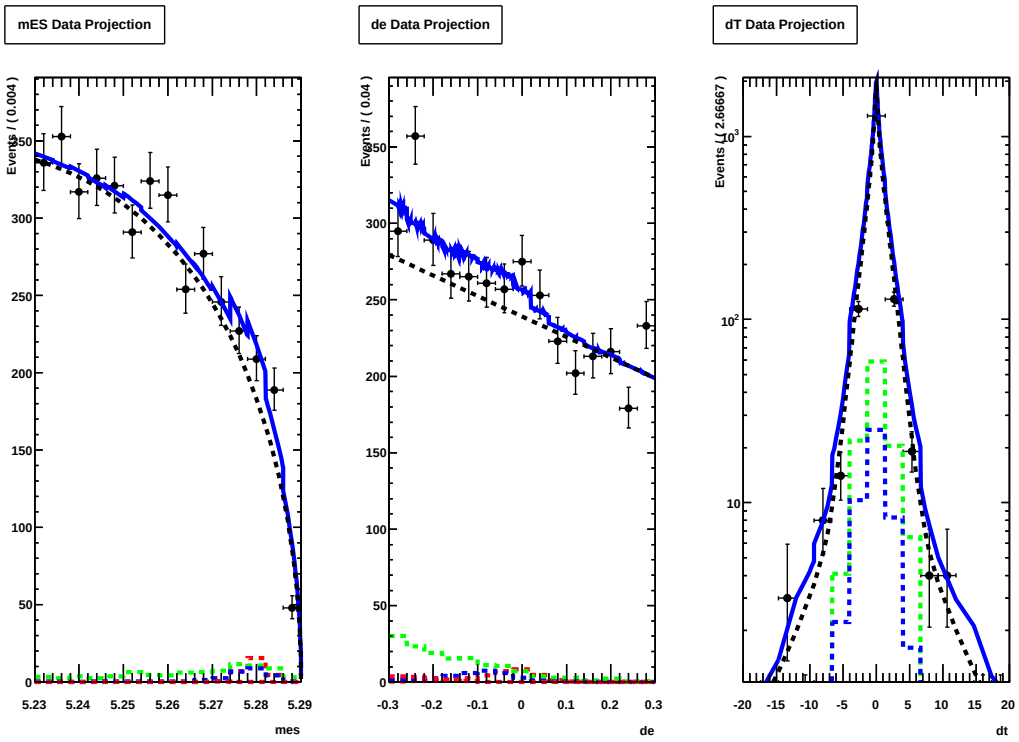

Figure 9.3: Shown above are, from left to right, $m_{\rm ES}$, ΔE^*, and Δt projections of the first stage fit with the data employing a BDT output > 0.5 cut. In each projection the red curve is the $B^0 \to \rho^0\gamma$ signal, the black curve is the continuum background, the green curve is the generic $B\overline{B}$ background, the blue curve is the first peaking cocktail, and the pink curve is the second peaking cocktail.

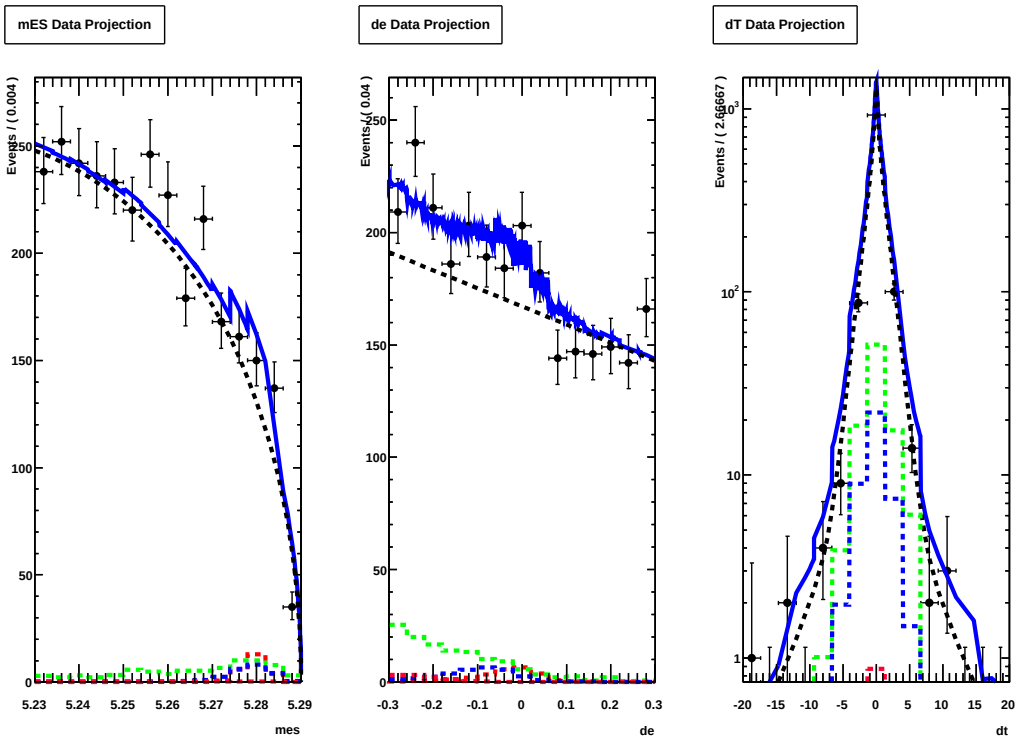

Figure 9.4: Shown above are, from left to right, $m_{\rm ES}$, ΔE^*, and Δt projections of the first stage fit with the data employing a BDT output > 0.6 cut. In each projection the red curve is the $B^0 \to \rho^0\gamma$ signal, the black curve is the continuum background, the green curve is the generic $B\overline{B}$ background, the blue curve is the first peaking cocktail, and the pink curve is the second peaking cocktail.

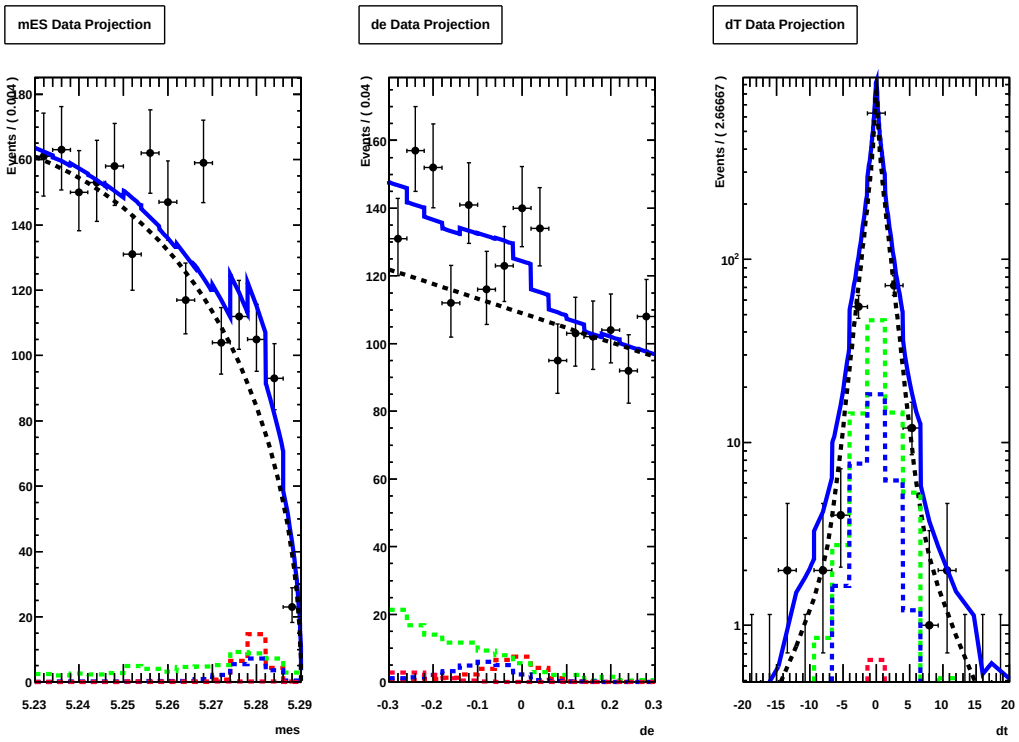

Figure 9.5: Shown above are, from left to right, $m_{\rm ES}$, ΔE^*, and Δt projections of the first stage fit with the data employing a BDT output > 0.7 cut. In each projection the red curve is the $B^0 \to \rho^0\gamma$ signal, the black curve is the continuum background, the green curve is the generic $B\overline{B}$ background, the blue curve is the first peaking cocktail, and the pink curve is the second peaking cocktail.

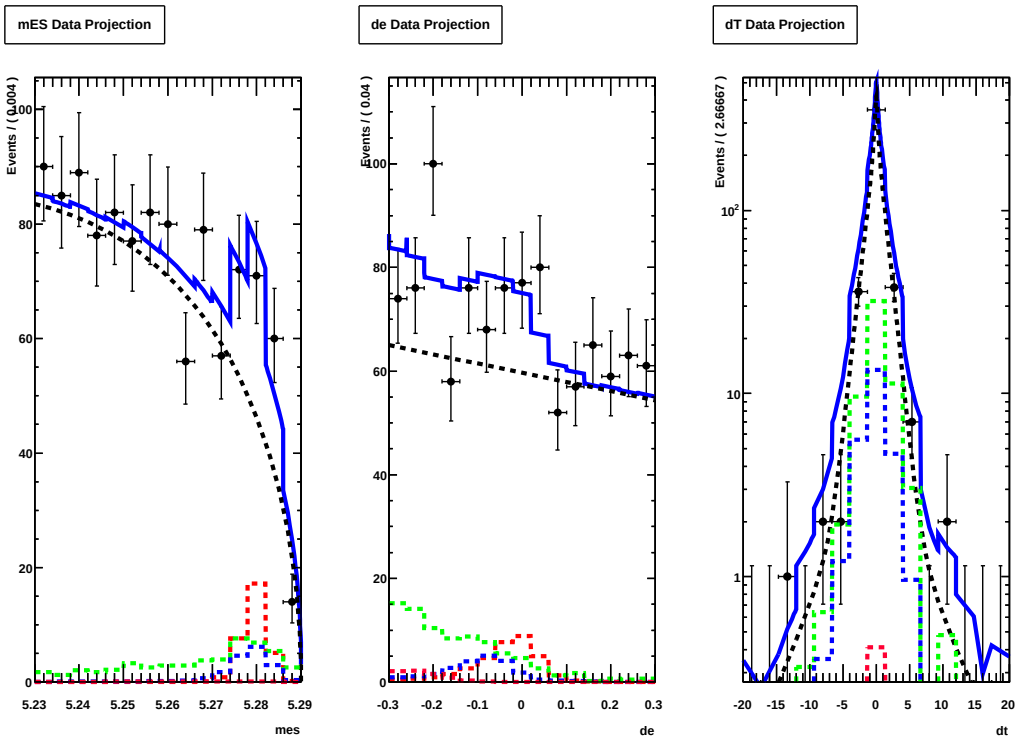

Figure 9.6: Shown above are, from left to right, $m_{\rm ES}$, ΔE^*, and Δt projections of the first stage fit with the data employing a BDT output > 0.8 cut. In each projection the red curve is the $B^0 \to \rho^0\gamma$ signal, the black curve is the continuum background, the green curve is the generic $B\overline{B}$ background, the blue curve is the first peaking cocktail, and the pink curve is the second peaking cocktail.

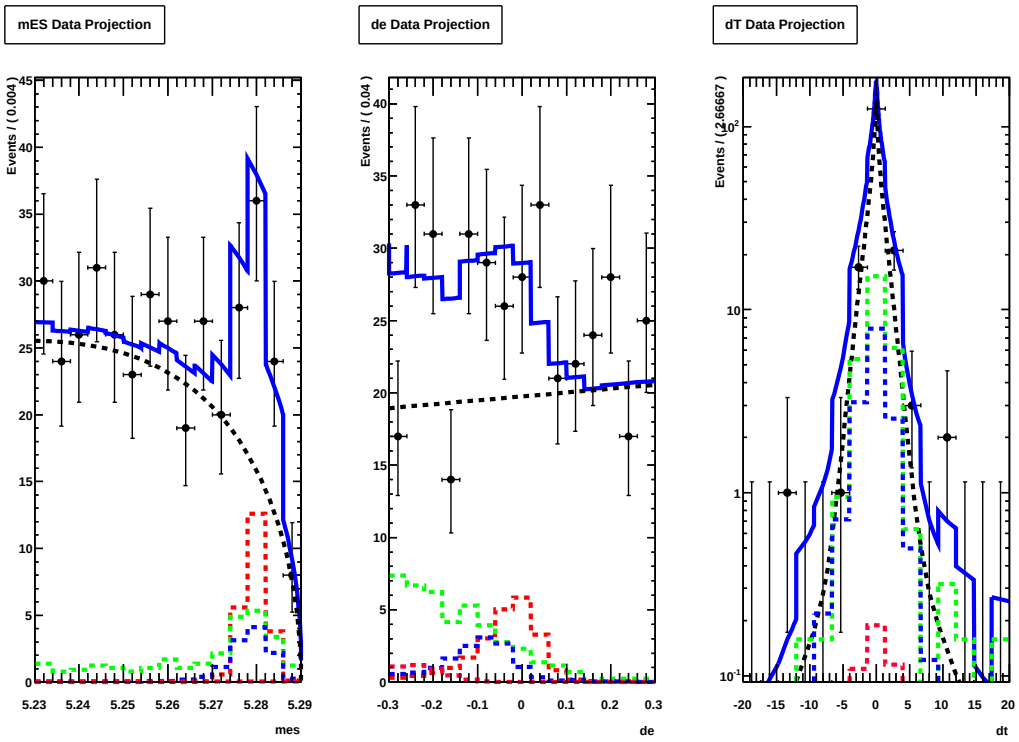

Figure 9.7: Shown above are, from left to right, $m_{\rm ES}$, ΔE^*, and Δt projections of the first stage fit with the data employing a BDT output > 0.9 cut. In each projection the red curve is the $B^0 \to \rho^0\gamma$ signal, the black curve is the continuum background, the green curve is the generic $B\overline{B}$ background, the blue curve is the first peaking cocktail, and the pink curve is the second peaking cocktail.

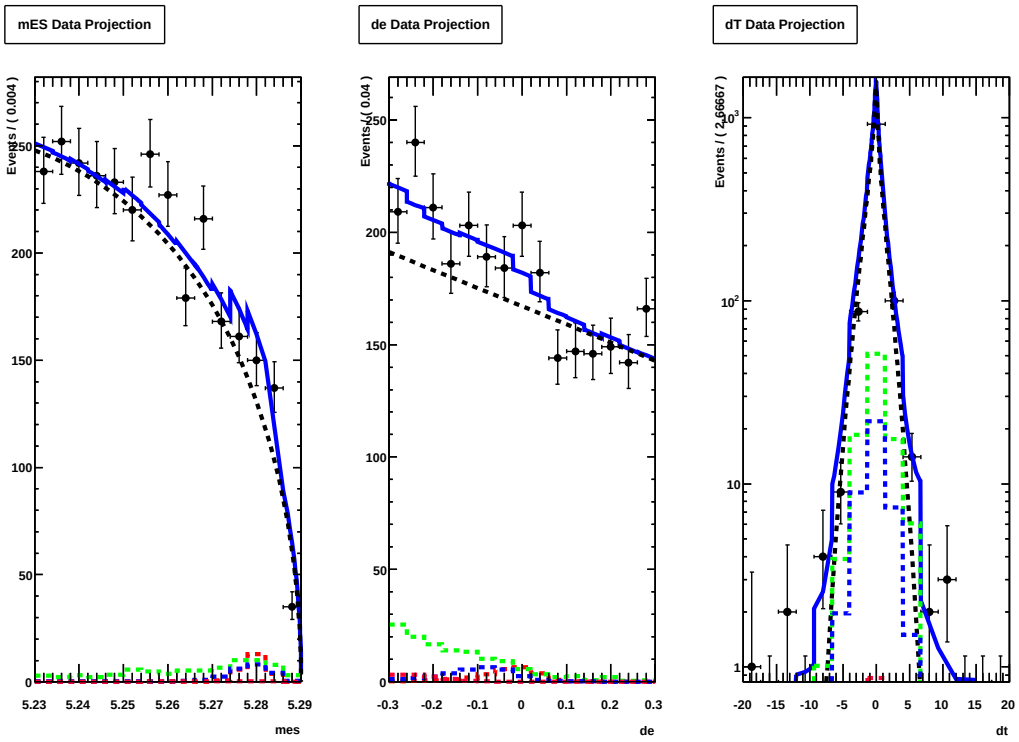

Figure 9.8: Shown above are, from left to right, $m_{\rm ES}$, ΔE^*, and Δt projections of the first stage fit with the data employing a BDT output > 0.6 cut and fixed Δt triple gaussian resolution function parameters. In each projection the red curve is the $B^0 \to \rho^0\gamma$ signal, the black curve is the continuum background, the green curve is the generic $B\overline{B}$ background, the blue curve is the first peaking cocktail, and the pink curve is the second peaking cocktail.

9.3 Remove Peaking $B\overline{B}$ Backgrounds From Fit

Since we have taken the shape, size, and fit variable dependence of the peaking backgrounds directly from the MC simulation systematic uncertainties have been introduced. To obtain a very conservative estimate of the size and uncertainty on S and C that arises from this assumption we have performed the first and second stage fits under the alternative assumption that the peaking backgrounds are absent, again making use of a BDT cut of 0.6 (see Figure 9.9). This leads to a change in S of 0.34 and in C of 0.24. Since this is a very conservative study we take half of these changes as an estimate of the range of systematic error due to possible modeling errors in the peaking backgrounds.

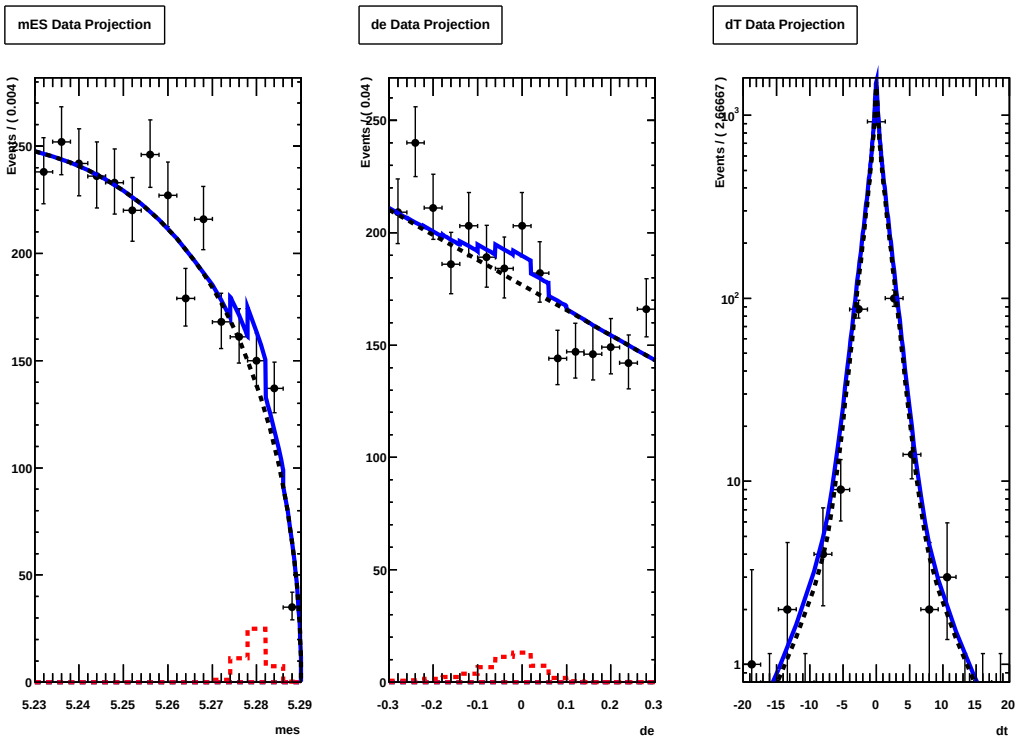

Figure 9.9: Shown above are, from left to right, $m_{\rm ES}$, ΔE^*, and Δt projections of the first stage fit with the data employing a BDT output > 0.6 cut and peaking backgrounds contributions set to zero. In each projection the red curve is the $B^0 \to \rho^0\gamma$ signal and the black curve is the continuum background.

9.4 Preliminary Systematic Uncertainties

Table 9.1 lists the signal yield, S, and C values with their corresponding uncertainties obtained from the three systematic uncertainty tests described in the previous sections. Combining these sources of systematics errors in quadrature, we arrive at the final preliminary values of S and C of

$$C = 0.79 \pm 0.51(\text{stat}) \pm 0.37(\text{sys}) \tag{9.1}$$

$$S = 0.38 \pm 0.54(\text{stat}) \pm 0.38(\text{sys}). \tag{9.2}$$

Although the systematic errors are significantly larger than those of the BELLE measurement [6], $S_{\rho^0\gamma} = -0.83 \pm 0.65(\text{stat}) \pm 0.18(\text{sys})$ and $C_{\rho^0\gamma} = 0.44 \pm 0.49(\text{stat}) \pm 0.14(\text{sys})$, the statistical accuracy is competitive. We are confident that a more rigorous determination of the systematic error, once the performance of the BDT cut is better understood, will make our measurement fully competitive with that of BELLE.

Varying BDT Cut	Signal Yield	S	C
0.3	22 ± 24	0.05 ± 0.56	1.08 ± 0.69
0.4	26 ± 22	0.45 ± 0.56	1.04 ± 0.04
0.5	32 ± 19	0.31 ± 0.47	1.05 ± 0.46
0.6	26 ± 16	0.38 ± 0.54	0.79 ± 0.51
0.7	29 ± 14	0.12 ± 0.54	0.61 ± 0.48
0.8	34 ± 13	0.55 ± 0.56	0.16 ± 0.40
0.9	23 ± 9	0.63 ± 0.58	-0.30 ± 0.43
Fixed Δt Parameters	26 ± 16	0.68 ± 0.23	0.81 ± 0.20
Continuum Backgrounds Only	50 ± 17	0.04 ± 0.35	0.55 ± 0.36

Table 9.1: Systematic studies performed: vary the BDT cut from 0.3 to 0.9, fix the core (100%) and outlier fractions (0%) in the signal and continuum background Δt resolution function and the continuum core and tail bias, and eliminate all backgrounds but the continuum in the final study. Listed above are the extracted yields and S and C values along with their errors after performing the two-stage fit with the data. Unless otherwise noted a BDT cut of 0.6 was used.

Chapter 10

Conclusion

Making use of the full runs 1-6 *BABAR* data-set of 465 million $B\overline{B}$ pairs we have done a preliminary measurement of the TDCPV parameters S and C in the decay of $B^0 \to \rho^0\gamma$, finding

$$C = 0.79 \pm 0.51(\text{stat}) \pm 0.37(\text{sys}) \tag{10.1}$$

$$S = 0.38 \pm 0.54(\text{stat}) \pm 0.38(\text{sys}). \tag{10.2}$$

These numbers provide a preliminary comparison with those of the BELLE collaboration, $S = -0.83 \pm 0.65(\text{stat}) \pm 0.18(\text{sys})$ and $C = 0.44 \pm 0.49(\text{stat}) \pm 0.14(\text{sys})$, using a sample of 657 million $B\overline{B}$ pairs collected with the BELLE detector. The statistical uncertainty of the two measurements is quite similar while *BABAR*'s systematic uncertainty is somewhat larger than that of BELLE. However, *BABAR*'s estimate of systematic error is merely preliminary, is rather conservative, and might

be expected to decrease as further studies are completed. Including systematic uncertainties the two collaborations' measured values of C are consistent within one standard deviation while the values of S exhibit a marginal disagreement of 1.4σ. The combined results of the two collaborations are consistent with the hypothesis of neither direct nor indirect CP-violation in the decay of $B^0 \to \rho^0\gamma$.

The measurement of the CP-violating parameters S and C presented here are preliminary and there are studies underway that may improve both the statistical and systematic precision of the measurement. The statistical accuracy is limited by the unexpectedly low yield of $B^0 \to \rho^0\gamma$ events. This is not understood and is under exploration via the reconstruction of the kinematically identical $B^0 \to K^{*0}\gamma$ ($K^{*0} \to K^+\pi^-$) signal. There is hope that this study will provide guidance as to how the $B^0 \to \rho^0\gamma$ yield can be increased. This in turn might be expected to reduce some of the observed variation of the extracted values of S and C as a function of the BDT cut reducing the dominant source of error on the determination of the C parameter. In addition, a more careful study of the decay difference time (Δt) resolution should allow a much more representative study of the dependence of the S parameter on the uncertainties of the reconstruction of Δt, thus allowing for the reduction of the overall systematic uncertainty of the S parameter. It is hoped that at the end of this process the *BABAR* measurement of S and C will exceed the accuracy of that of the BELLE collaboration's measurement.

Bibliography

[1] See, for example, S. Bertolini, F. Borzumati and A. Masiero, Nucl. Phys. B **294**, 321 (1987); H. Baer, M. Brhlik, Phys. Rev. D **55**, 3201 (1997) [arXiv:hep-ph/9610224]; J. L. Hewett, J. D. Wells, Phys. Rev. D **55**, 5549 (1997) [arXiv:hep-ph/9610323]; M. S. Carena, D. Garcia, U. Nierste and C. E. M. Wagner, Phys. Lett. B **499**, 141 (2001) [arXiv:hep-ph/0010003].

[2] D. Mohapatra *et al.* [BELLE Collaboration], Phys. Rev. Lett. **96**, 221601 (2006). [arXiv:hep-ex/0506079].

[3] K. Abe *et al.* [BELLE Collaboration], Phys. Rev. D **74**, 221601(R) (2006).

[4] B. Aubert *et al.* [*BABAR* Collaboration], Phys. Rev. Lett. **98**, 151802 (2007) [arXiv:hep-ex/0612017].

[5] B. Aubert *et al.* [*BABAR* Collaboration], Phys. Rev. D **72**, 051103(R) (2005).

[6] Y. Ushiroda *et al.*, Phys. Rev. Lett. **100** 021602 (2008) [arXiv:hep-ex/0709.2769].

[7] S. L. Glashow, Nucl. Phys. **22**, 579 (1961).

[8] S. Weinberg, Phys. Rev. Lett. **19**, 1264 (1967).

[9] A. Salam, Originally printed in Svartholm: Elemetary Particle Theory, Proceedings Of The Nobel Symposium Held 1968 At Lerum, Sweden, Stockholm 1968, 367-377.

[10] P. W. Higgs, Phys. Rev. Lett. **13**, 508 (1964).

[11] N. Cabibbo, Phys. Rev. Lett. **10**, 531 (1963).

[12] M. Kobayashi and T. Maskawa, Prog. Theor. Phys. **49**, 652 (1973).

[13] L. Wolfenstein, Phys. Rev. Lett. **51**, 1945 (1983).

[14] D. Du *et al.*, Phys. Rev. Lett. **59**, 1072-1075 (1987)

[15] K. Nakamura *et al.*, (Particle Data Group) J. Phys. G **37**, 050021 (2010).

[16] A. Ali and A. Y. Parkhomenko, Eur. Phys. J. C **23**, 89 (2002) [arXiv:hep-ph/0105302].

[17] J. Rosner, (2002), [arXiv:hep-ph/0306284v2].

[18] B. Aubert *et al.* [*BABAR* Collaboration], (2001), [hep-ex/0105044].

[19] G. Sciolla *et al.*, (2006), *BABAR* Publications Board, *BABAR* Analysis Document **1301**.

[20] P. Ball *et al.*, Phys. Rev. D **75**, 054004 (2007).

[21] A. Ali *et al.*, Phys. Lett. B **595**, 323 (2004); C. D. Lu *et al.*, Phys. Rev. D **72**, 094005 (2005) [Erratum-ibid. D **73**, 039902 (2006)].

[22] *BABAR*, P. F. Harrison and H. R. Quinn, editors, *The BaBar Physics Book: Physics at an asymmetric B factory*, 1998, Papers from Workshop on Physics at an Asymmetric B Factory (BaBar Collaboration Meeting), Rome, Italy, 11-14 Nov 1996, Princeton, NJ, 17-20 Mar 1997, Orsay, France, 16-19 Jun 1997 and Pasadena, CA, 22-24 Sep 1997.

[23] D. J. Lange, Nucl. Instrum. Meth. A **462**, 152 (2001).

[24] GEANT4 Collaboration, S. Agostinelli *et al.*, Nucl. Instrum. Meth. A **506**, 250 (2003).

[25] G. C. Fox and S. Wolfram, Phys. Rev. Lett. **41**, 1581 (1978).

[26] T. Hadig *et al.*, (2004), *BABAR* Publications Board, *BABAR* Analysis Document **876**.

[27] T. Piatanko *et al.*, (2008), *BABAR* Publications Board, *BABAR* Analysis Document **1693**.

[28] J. Friedman and N. Fisher, *Bump hunting in high dimensional data, Statistics and Computing*, **9**, 123 (1999).

[29] I. Narsky, *StatPatternRecognition: A C++ Package for Statistical Analysis of High Energy Physics Data*, physics/0507143, (2005).

[30] W. Verkerke and D. Kirkby, "The RooFit Toolkit for Data Modeling", http://roofit.sourceforge.net/.

[31] J. Tuggle *et al.*, (2008), *BABAR* Publications Board, *BABAR* Analysis Document **1740**.

[32] K. George *et al.*, (2007), *BABAR* Publications Board, *BABAR* Analysis Document **1447**.

[33] V. Lombardo *et al.*, (2008), *BABAR* Publications Board, *BABAR* Analysis Document **2082**.